Angewandte Chemie
Eine Zeitschrift der Gesellschaft Deutscher Chemiker

Supporting Information

Rigid Arrangements of Ionic Charge in Zeolite Frameworks Conferred by Specific Aluminum Distributions Preferentially Stabilize Alkanol Dehydration Transition States

Alexander J. Hoffman, Jason S. Bates, John R. Di Iorio, Steven V. Nystrom, Claire T. Nimlos, Rajamani Gounder, and David Hibbitts**

anie_202007790_sm_miscellaneous_information.pdf

Supporting Information

Table of Contents

List of Figures

S1. Computational methods

Fully periodic, dispersion-corrected density functional theory (DFT) calculations were performed using the Vienna ab initio simulation package (VASP)[1–4] in the computational catalysis interface (CCI).[5] Planewaves were constructed using the projector augmented wave (PAW) method with an energy cutoff of 400 eV.[6,7] The Perdew-Burke-Ernzerhof (PBE) form of the generalized gradient approximation (GGA) with the DFT-D3 correction with Becke-Johnson damping (D3BJ) was used for all calculations.[8–10] The Brillouin zone was sampled at the Γ-point. Calculations were converged in a two-step process, which is ~3× more efficient than traditional single-step DFT calculations sampled at the Γ-point.[5] In the first step, wavefunctions were converged such that energies differed by $<10^{-4}$ eV between iterations and forces on all atoms were < 0.05 eV $Å^{-1}$, as determined using a fast Fourier transform (FFT) grid with a cutoff 1.5× that of the planewave cutoff (PREC = .NORMAL. in VASP). Structures were reoptimized in a second step such that wavefunctions were converged to within 10^{-6} eV $Å^{-1}$ and until the maximum force on each atom was < 0.05 eV $Å^{-1}$ as calculated with an FFT grid 2× the planewave cutoff (PREC = .ACCURATE. in VASP).

Transition state searches were initiated by a nudged elastic band (NEB) calculation composed of 16 images and were converged such that the maximum force on each atom did not exceed 0.5 eV $Å^{-1}$.[11,12] These transition states were refined using the dimer method.[13] Dimer calculations were converged using the same criteria as those used for optimizations (electronic energy difference < 10^{-6} eV, structural force maximum of 0.05 eV $Å^{-1}$) in a similar multi-step process. Partial charges on atoms in converged optimization, NEB, and Dimer calculations were computed using the quasiatomic minimal basis orbital (QUAMBO) method.[14]

Frequency calculations were performed on all converged gas-phase, adsorbed, and transition state species. These frequency calculations used a fixed displacement method with two displacements to approximate zero-point vibrational energies (ZPVE), enthalpies (H), and free energies (G) at 415 K and 1 bar (standard pressure). Enthalpies and free energies are considered a sum of DFT-calculated electronic energy, ZPVE, and vibrational, rotational, and translational enthalpies (H_{vib}, H_{rot}, H_{trans}) or free energies (G_{vib}, G_{rot}, G_{trans})

$$H = E_0 + ZPVE + H_{trans} + H_{rot} + H_{vib} \tag{S1}$$

$$G = E_0 + ZPVE + G_{trans} + G_{rot} + G_{vib} \tag{S2}$$

Any motions of adsorbates and transition states in zeolite frameworks were considered vibrations (i.e., translational and rotational contributions are zero for non-gas-phase species). All framework Si and O atoms were frozen in place during frequency calculations, except for O atoms attached to framework Al atoms. Low-frequency vibrations (frustrated translational and rotational motions) disproportionately affect entropy estimates; frequencies below 60 cm^{-1}—unless associated with the motion along the reaction coordinate for a transition state—were replaced with 60 cm^{-1} to mitigate these inaccuracies, as in previous work.[15,16] Vibrational energies, enthalpies, and free energies were calculated from statistical mechanics:[17]

$$ZPVE = \sum_i \left(\frac{1}{2} h\nu_i\right) \tag{S3}$$

$$H_{vib} = \sum_i \left(\frac{h\nu_i \exp\left(-\frac{h\nu_i}{kT}\right)}{1-\exp\left(-\frac{h\nu_i}{kT}\right)}\right) \tag{S4}$$

$$H_{vib} = \sum_i \left(-kT \ln\left(\frac{1}{1-exp\left(-\frac{h\nu_i}{kT}\right)}\right)\right) \tag{S5}$$

Translational and rotational enthalpies and free energies are calculated for all gas-phase species from the same principles:

$$H_{trans} = \frac{5}{2} k_B T \tag{S6}$$

$$H_{rot,linear} = k_B T \tag{S7}$$

$$H_{rot,nonlinear} = \frac{3}{2} k_B T \tag{S8}$$

$$G_{trans} = -k_B T \ln\left(\left(\frac{2\pi M k_B T}{h^2}\right)^{\frac{3}{2}} V\right) \tag{S9}$$

$$G_{rot} = -k_B T \ln\left(\frac{\pi^{\frac{1}{2}}}{\sigma}\left(\frac{T^3}{\theta_x \theta_y \theta_z}\right)^{\frac{1}{2}}\right) \tag{S10}$$

$$\theta_i = \frac{h^2}{8\pi^2 k_B I_i} \tag{S11}$$

where I_i is the moment of inertia about each axis for species i and σ is its symmetry number. Entropies (S) are calculated from H and G:

$$S = \frac{H-G}{T} \tag{S12}$$

at 415 K.

The CHA structure was obtained from the IZA database ($a = b = 13.675$ Å, $c = 14.125$ Å; $\alpha = \beta = 90°$, $\gamma = 120°$).[18] Other zeolite frameworks—predominantly MFI—are prone to restructuring during DFT calculations, leading to artifacts that affect catalytic predictions; however, CHA is not prone to such artifacts.[19] CHA has only one symmetrically unique T-site, with four symmetrically unique O atoms bound to each T-site (Figure 1a, main text). Each T-site in CHA is in three distinct voids and is contained in six rings: three four-membered rings (4-MR), a 6-MR, and two 8-MR. Each 8-MR around a T-site contains two of its O atoms: one includes O2 and O3 (8-MR(2,3)) and the other O2 and O4 (8-MR(2,4); Fig. 1, main text). Calculations were completed with only one Al substituted in the CHA unit cell (site *A* in Figure 3, main text) and with two Al substituted in proximal positions sharing the 6-MR of CHA (one at site *A* and another at site *C*, *D*, or *E*). These site-pairs are denoted *AC*, *AD*, and *AE*, respectively, and the names of these site pairs conform to those used in previous work.[20] Site-pairs *AB* and *AF* were not considered because they violate Löwenstein's rule,[21] although previous work has indicated that *AB* and *AF* site-pairs are stable in H-form CHA.[22,23] The Al atoms in the *AD* site-pair configuration share two rings (the 6-MR and the 8-MR(2,4) of the *A* site) in the CHA structure as a result of periodic boundary conditions. This periodicity results in interactions between these sites that are not exclusively across 6-MR structures.

The effects of Si:Al ratio on Step S1 barriers were analyzed by systematically adding Al to 23 previously identified key locations in the CHA framework (see Section S12 for details) without violating Löwenstein's rule to a methanol monomer on O3 (not its most stable location on O4)[16] and the Step S1 transition state on O3. Al was added such that the Si:Al ratio decreased from 35 (1 Al in the CHA unit cell) to 6.2 (5 Al in the CHA unit cell). Each structure was reoptimized upon addition of another Al. No coadsorbates were added to new Al atoms and protons on new Al remained bare. Structures were calculated with the proton on all four O atoms of a newly added Al while proton locations on previously added Al were kept fixed.

S2. Chabazite samples and dehydration kinetics measurements

H-CHA zeolites were hydrothermally synthesized and tchoroughly characterized in prior work[24,25] to have 0%, 23%, and 44% of their H^+ in paired configurations by divalent Co^{2+} titration (Table S1). These samples will be referred to as H-CHA(X), where X is the fraction of paired H^+. Si-CHA was also synthesized in prior work.[24]

Table S1. H-CHA zeolites studied.[a]

Zeolite Name	H^+ density[b] / 10^{-4} mol g^{-1}	H^+/Al[b]	Al_f/Al_{total}[c]	Co/Al[c]	Al_{pair}/Al_{tot}[d]
H-CHA(0.44)	8.4	0.83	0.83	0.22	0.44
H-CHA(0.23)	11	1.02	0.88	0.12	0.23
H-CHA(0)	9.6	0.96	0.95	0	0

[a]Characterization data on these CHA zeolites has been reported in the literature.[24–26]
[b]Quantified by NH_3-TPD
[c] [c]Fraction of framework Al (Al_f) per total Al (Al_{total}) measured by ^{27}Al MAS NMR.[24]
[d]Quantified by AAS after aqueous-phase ion-exchange saturation as reported for CHA[25]
[e]Al_{pair} reflects H^+ titrated by Co^{2+} in 6-MR in CHA zeolites.

Methanol dehydration kinetics were measured using a packed-bed reactor, operated at <10% conversion, described previously.[16,24] Briefly, 0.005-0.030 g of CHA zeolite (180-250 μm diameter) were diluted with Si-CHA to obtain a minimum solid mass of 0.025 g and held between two plugs of quartz wool. The fresh catalyst powder was heated to 773 K (0.033 K s^{-1}) in flowing 5% O_2 with He as the balance gas (50 cm^3 g^{-1} s^{-1}, 99.999%, Indiana Oxygen) for 4 hours and then cooled to 415 K. The reactor was then purged with dry He (150 cm^3 g^{-1} s^{-1}, 99.999%, Indiana Oxygen) prior to introduction of methanol (99.9 wt %, Sigma-Aldrich) via heated transfer lines (>373 K) using a syringe pump (Legato 100, KD Scientific). Methane (25% CH_4/Ar, 99.999%, Indiana Oxygen) was introduced into the reactor effluent stream for use as an internal standard (0.083 cm^3 s^{-1}) and this stream was sent to a gas chromatograph equipped with a flame ionization detector (HP Plot-Q KCl column, 0.53 mm ID × 30 m × 40 μm film, Agilent).

Ethanol dehydration kinetics were measured in a differential packed-bed reactor apparatus described previously.[27,28] Zeolites were pelleted, crushed, and sieved to retain aggregates between 180–250 μm. An intrapellet mixture of H-CHA(0.44) with Si-CHA (17 wt% H-CHA) was similarly prepared in order to maintain differential conversions with lower catalyst loading. Samples (0.005 g) were loaded into a quartz tube (7 mm I.D.) and supported between two plugs of acid-washed quartz wool (W. R. Grace, washed with 1 M HNO_3 for 16 h at ambient temperature), and the bed was further diluted with Si-CHA to a total mass of 0.021–0.026 g. The quartz tube was held within a three-zone furnace (Applied Test Systems) equipped with Watlow controllers. A K-type thermocouple (Omega) held in contact with the outside of the quartz tube at the level of the bed was used to monitor the reaction temperature. Zeolites were first treated in flowing 5% O_2/He (UHP, Indiana Oxygen, 50 cm^3 (g zeolite)$^{-1}$ s^{-1}) for 4 h at 773 K (0.0333 K s^{-1}), then cooled in flowing He (UHP, Indiana Oxygen, 50 cm^3 (g zeolite)$^{-1}$ s^{-1}) to 415 K, and held at this temperature for 1 h before introducing the reactant feed. Liquid ethanol (Sigma-Aldrich, anhydrous, >99.5%) loaded within a gastight glass syringe (Hamilton 1000 series) was fed via syringe pump (KD Scientific Legato 100) and vaporized into a flowing He stream heated to >383 K. The concentrations of ethanol and reaction products (diethyl ether, ethene) were quantified by an on-line gas chromatograph (Agilent 6890) equipped with a capillary column (HP-PLOT-Q, 30 m × 530 μm × 40 μm) and flame ionization detector. The concentration of the reactant feed was verified via GC injections in a line bypassing

the reactor. Reaction rates were quantified at steady-state after remaining at one ethanol pressure condition for 4 h, and represent the average of the last 1.5 h of GC injections. Ethanol pressure (0.05–69 kPa) was varied non-systematically over the course of the experiment, and no deactivation was observed as verified by periodic rate measurements at a reference condition (5 kPa ethanol). Conversions were < 3% for all the reported rate data.

S3. MFI, AEI, LEV, and LTA zeolite structures

Zeolites are ubiquitous in industrial chemical processes, specifically in alkane cracking during petrochemical refinement. The most common zeolite used for this process is MFI,[29,30] which has straight and sinusoidal 10-MR pores that intersect to form larger voids (Figure S1). High-temperature, orthorhombic MFI has 12 unique T-sites and 26 unique O atoms.[31] The characteristic void sizes of MFI differ from those of CHA; where CHA has a window-cage topology (3.7 Å windows, 7.4 Å × 9.8 Å cages),[32] the wider straight (5.3 Å × 5.6 Å) and sinusoidal (5.5 Å × 5.1 Å) channels intersect to form voids slightly larger than those of CHA (7.0 Å × 10.7 Å).[32,33]

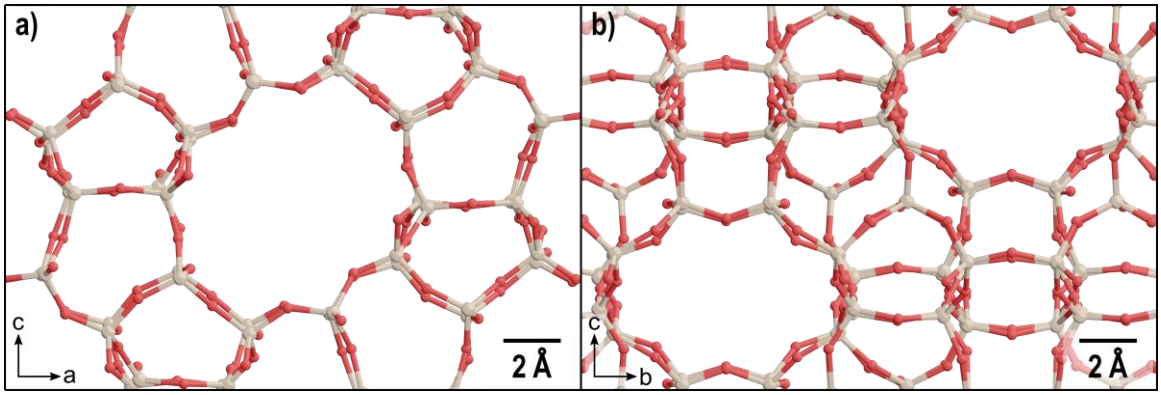

Figure S1. The MFI structure shown along (a) the straight channel (the [010] vector) and (b) the sinusoidal channel (the [100] vector).

AEI (a = 13.677 Å, b = 12.607 Å, c = 18.497 Å, $\alpha = \beta = \gamma$ = 90.0°), LEV ($a = b$ = 13.168 Å, c = 22.578 Å, $\alpha = \beta$ = 90.0°, γ = 120.0°), and LTA ($a = b = c$ = 11.919 Å, $\alpha = \beta = \gamma$ = 90.0°) zeolites are small-pore zeolites similar to CHA, with adjacent 6- and 8-MR windows, the latter of which lead into larger cage voids (Figure S2–S3). AEI and LEV also have the same stacked double-6-MR motif found in CHA frameworks. The 8-MR are similar sizes to those in CHA for AEI (3.8 Å) and LTA (4.1 Å); LEV, however, has asymmetric 8-MR windows (3.6 Å × 4.8 Å).[32] These small-pore zeolite frameworks also have high-symmetry similar to CHA; AEI (3 T-sites), LEV (2 T-sites), and LTA (1 T-site) all have few unique T-sites. The systematic control of Al distribution in these frameworks, however, has not been achieved as it has for CHA.[25]

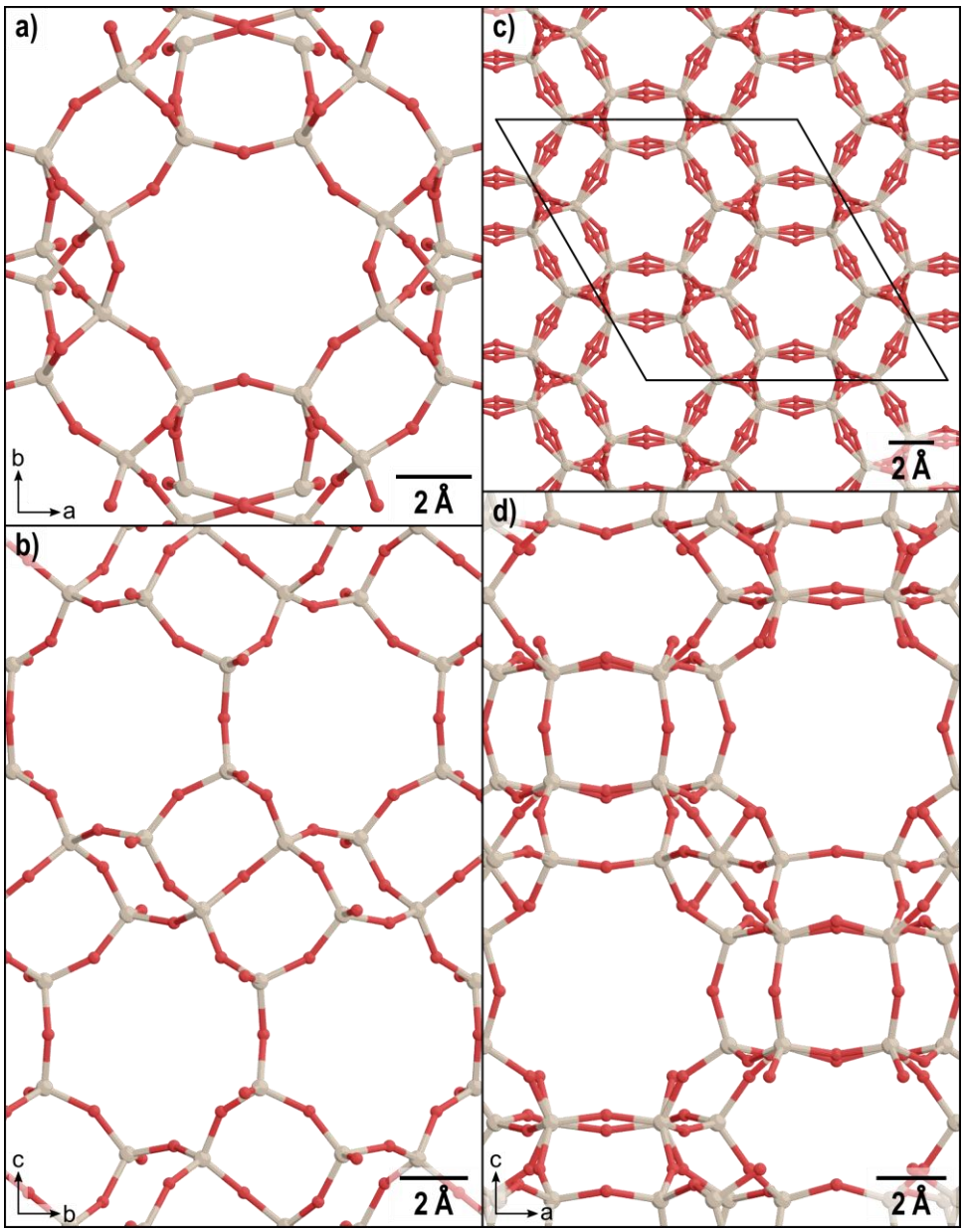

Figure S2. The structures of (a) AEI down the *c* vector, (b) AEI down the *a* vector, (c) LEV down the *c* vector (with its unit cell outlined in black), and (d) LEV in the plane formed by the *a* and *c* vectors.

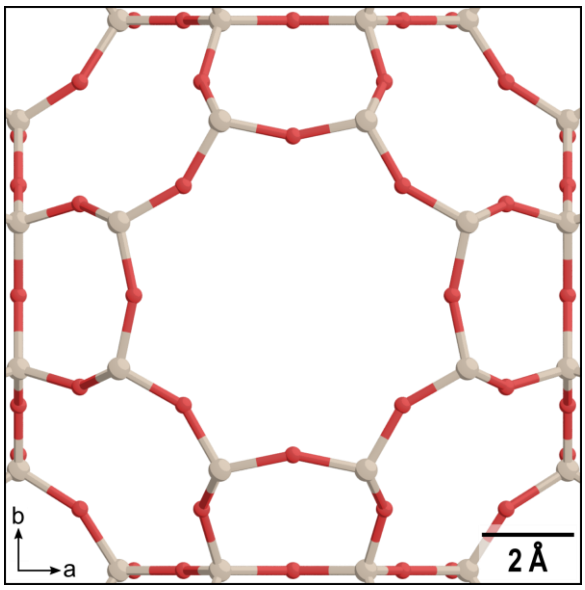

Figure S3. The structure of LTA along the *c* vector. Because of the high symmetry of LTA, views along its other unit cell vectors look identical.

S4. Comparison and equivalence of next-nearest neighbor site-pairs AC *and* AE

The *AC* and *AE* site-pairs examined in this work are both next-nearest neighbor (NNN) configurations and have AlO_4^- tetrahedra separated by one bridging Si atom (Figure S4). If a reaction occurs exclusively at the *A* site in these configurations, they are distinct. The O atom on the *C* site nearest the reacting *A* site is O1, while on the *E* site it is O3. This difference changes the way in which these sites interact upon deprotonation of the *A* site; the *AC* site-pair forms a stronger acid in this case because the remaining proton prefers to orient in the plane of the 6-MR shared by the Al (Figure 2, main text). The preferred configuration in the conjugate base of the *AE* site-pair, however, contains a proton on O3 of the *E* site, where it cannot H-bond with the deprotonated *A* site. As such, the DPE remains practically unchanged relative to an isolated site (ΔDPE = −1 kJ mol^{-1}). When the remaining proton binds to O1 of the *E* site, the conjugate base is not further stabilized as in the *AC* and *AD* site-pairs and the DPE increases relative to a bare site (ΔDPE = +8 kJ mol^{-1}; Figure S5b).

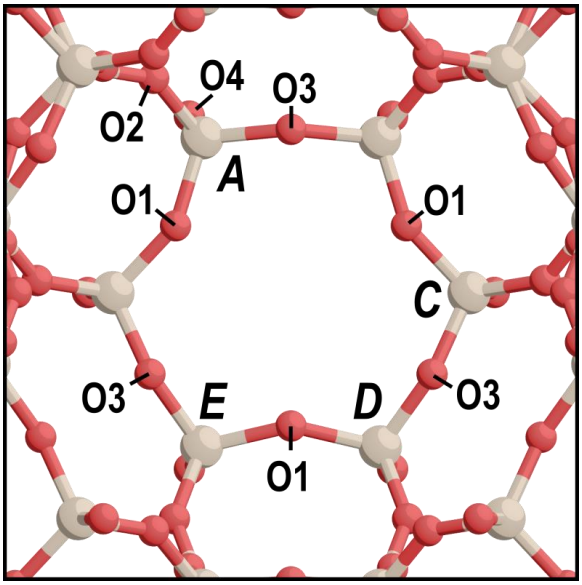

Figure S4. The sites evaluated in this work. Si^{4+} atoms were replaced by Al at the *A* position and at the *C*, *D*, and *E* positions to form *AC*, *AD*, and *AE* site-pairs, respectively. The O atoms attached to the *A* site are labeled according to convention.

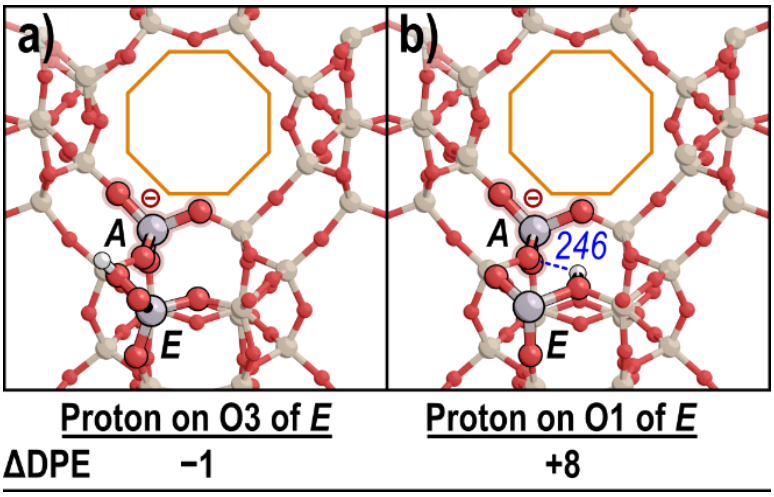

Figure S5. Difference in DPE in kJ mol^{-1} between the A site and the *AE* site pair when the remaining proton on the *E* site of the conjugate base is on (a) O3 and (b) O1.

DPE is a purely theoretical metric for acid strength. The site whose proton is removed can be explicitly controlled in these calculations. In synthesized materials, however, the location at which reactions occur is not fixed. As such, reactions could occur at either the *A* or *C* site in the *AC* site-pair or at the *A* or *E* site in the *AE* site-pair in H-SSZ-13 materials that have such NNN Al configurations. Therefore, the rate at a given site-pair (r_{AX}) is the sum of the rates at each site while the other site is not reacting (assuming they will not concurrently catalyze reactions):

$$r_{AC} = \frac{(r_{AC}+r_{CA})}{2} \tag{S13}$$

$$r_{AD} = \frac{(r_{AD}+r_{DA})}{2} \tag{S14}$$

$$r_{AE} = \frac{(r_{AE}+r_{EA})}{2} \tag{S15}$$

where r_{AX} is the rate at the *A* site with a nearby unreacting *X* site and r_{XA} is the rate at site *X* with a nearby unreacting *A* site. The assumption that both sites will not catalyze reactions simultaneously (i.e., transition states will not form on both sites concurrently) is valid if transition states are short-lived and form relatively infrequently. The *AD* site-pair, which forms a next-next-nearest neighbor Al arrangement (NNNN), is symmetric about the 6-MR; the *A* and *D* sites can interact in the same way across the 6-MR regardless of the site on which a reaction occurs. Therefore, $r_{A-D} = r_{D-A}$ and

$$r_{AD} = r_{NNNN} = \frac{(r_{AD}+r_{AD})}{2} = r_{AD} \tag{S16}$$

The NNN site-pair arrangements, however, are not perfectly symmetric because of the differences in their O atom locations (i.e, $r_{AX} \neq r_{XA}$ for a single site-pair). These site-pairs become identical, however, if reactions on the *C* and *E* sites in each site-pair are considered. For example, deprotonation of the *C* site in the *AC* site would be equivalent to deprotonation of the *A* site in the *AE* site-pair because their respective arrangements are symmetric. Similarly, deprotonation of the *E* site in the *AE* site-pair is equivalent to deprotonation of the *A* site in the *AC* site-pair. Therefore, the rate on the *E* site with the *AE* site-pair arrangement should be equivalent to the rate on the *A* site with the *AC* site-pair arrangement. Thus, the rates on any NNN Al arrangement sharing 6-MR should be

$$r_{NNN} = r_{AC} = r_{AE} = \frac{(r_{AC}+r_{AE})}{2} = \frac{(r_{AE}+r_{AC})}{2} \tag{S17}$$

because $r_{AC} = r_{EA}$ and $r_{AE} = r_{CA}$. Thus, we consider only the preferred reaction pathway on each NNN Al arrangement.

S5. Changes in free energy barriers for methanol dehydration with a bare paired site

While methanol dehydration occurs with sites entirely covered by clusters of one or more methanol at relevant conditions in CHA,[16,24] the effects of a nearby bare proton are still relevant to other Brønsted acid-catalyzed reactions which occur at low coverages (e.g., alkane cracking)[34–47]. Here, we analyze the effects of a nearby proton on the reaction energetics of methanol dehydration on each of the site-pairs analyzed in this work: *AC* (NNN), *AD* (NNNN), and *AE* (NNN).

The proton on the second unreacting site orients itself in the same position as in the conjugate base formed upon deprotonation (Figure 3, main text) in each of the preferred transition states found on these site-pairs (Figure S6). The presence of this proton, however, appears to confer no benefit to methanol dehydration and does not reduce the overall barriers for any route on any site-pair. The calculated overall barriers for surface methylation (Step S1) increase by 6, 1, and 1 kJ mol^{-1} on the *AC*, *AD*, and *AE* site-pairs, relative to an isolated site ($\Delta G^{\neq}$ = 135 kJ mol^{-1}). This slight increase in the overall barrier likely arises from the shift in the preferred location of the transition state from 8-MR(2,3)—where O3 was methylated—to 8-MR(2,4)—where O4 is instead methylated—on the *AC* and *AD* site-pair. The transition state is better stabilized in 8-MR(2,3) when methylating O3 than by 8-MR(2,4), but the presence of the nearby proton leads to unfavorable interactions between the cationic transition state and the proton. These interactions encourage the formation of the transition state in 8-MR(2,4). The overall barriers for this transition state on O4 of the *A* site for the *AC* and *AD* are lower than on O4 of the isolated site, indicating that the nearby proton does stabilize the conjugate base of the reacting site but its benefits are nullified by the less favorable transition state location (see Section S6). The *AC* and *AD* site-pairs allow for interactions between the proton on the second site and the reacting *A* site; the geometry of the *AE* site-pair, however, disfavors this interaction. As such, the transition state remains in 8-MR(2,3) on the *AE* site-pair and the nearby proton points away from the reacting A site. Because the original transition state geometry is maintained on the *AE* site-pair and there are no strong interactions between the nearby proton and the conjugate base of the reacting site, the overall barrier remains practically unchanged for surface methylation on *AE* ($\Delta G^{\neq}$ = 136 kJ mol^{-1}) compared to an isolated site ($\Delta G^{\neq}$ = 135 kJ mol^{-1}).

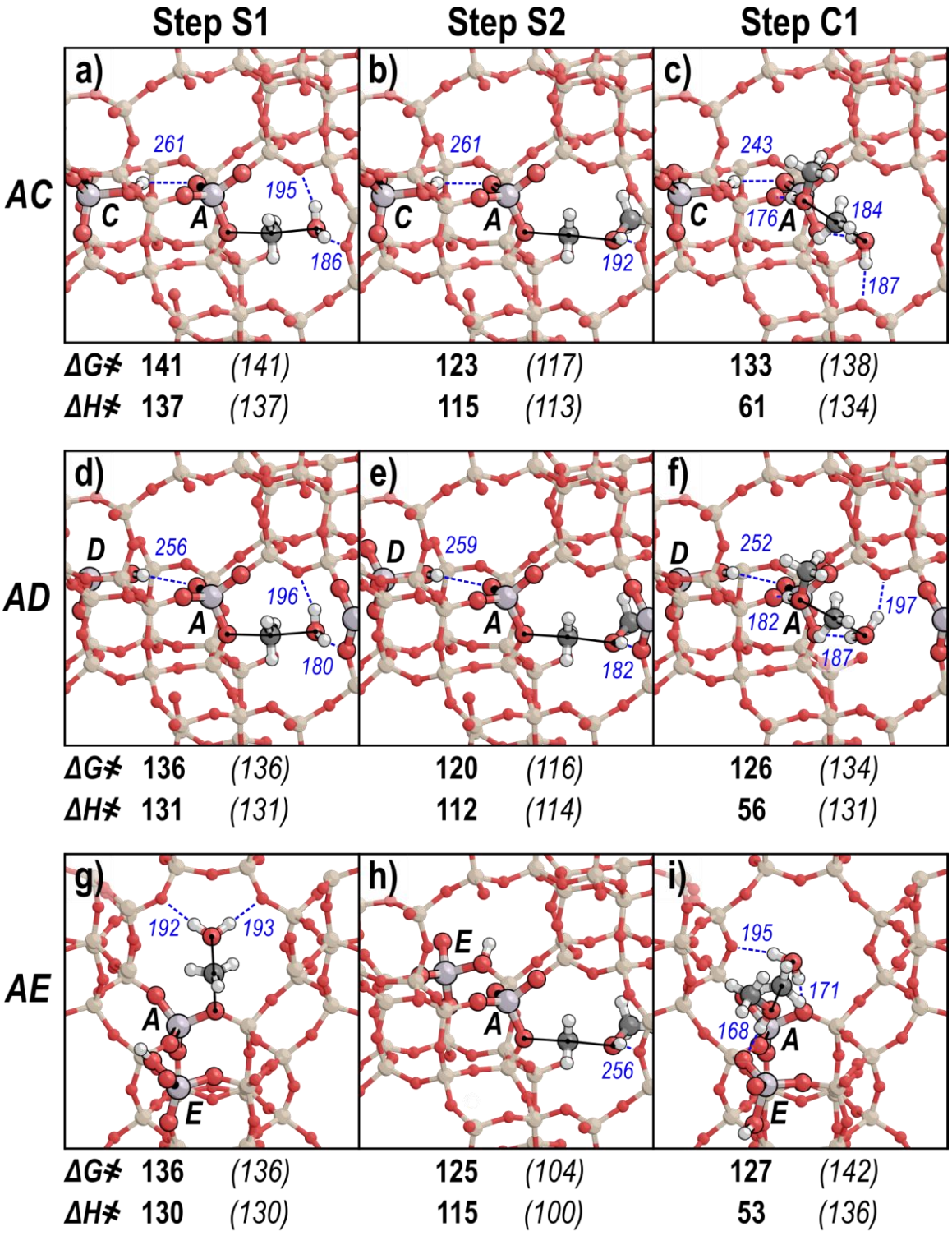

Figure S6. The most favorable transition state structures found for methanol dehydration in CHA for Step S1 (a,d,g), Step S2 (b,e,h), and Step C (c,f,i) for site-pairs in the *AC* (a,b,c), *AD* (d,e,f) and *AE* (g,h,i) arrangements with only a proton on the *C*, *D*, or *E* site. Their effective free energy and enthalpy barriers ($\Delta G^{\neq}$ and $\Delta H^{\neq}$) and their intrinsic barriers (ΔG_{act} and ΔH_{act} in parenthesis and italicizes) are shown in kJ mol^{-1}. Solid black lines indicate incipient and breaking bonds while blue dashed lines indicate H-bonds, whose lengths are labeled in pm.

Kinetically irrelevant methanol methylation (Step S2), however, has a lower overall barrier on each of these site-pairs, decreasing by 7, 10, and 5 kJ mol^{-1} on *AC*, *AD*, and *AE* relative to an isolated site ($\Delta G^{\neq}$ = 130 kJ mol^{-1}). This transition state prefers to occupy 8-MR(2,4) on the isolated site, a configuration which remains uninterrupted by the presence of a nearby site. Therefore, a proton on a nearby site serves to stabilize this methanol methylation transition state rather than hinder its formation. Again, the overall barriers for this reaction are lowest on the *AC* and *AD* site-pairs, in which the nearby proton bonds to O1 of the second site. Furthermore, the periodic boundary conditions create another Al in the 8-MR(2,4) which contains the transition state on the *AD* site-pair; such an additional interaction further stabilizes this cationic moiety.

Finally, overall Step C1 barriers increase by 10, 3, and 4 kJ mol^{-1} for *AC*, *AD*, and *AE* relative to the isolated site ($\Delta G^{\neq}$ = 123 kJ mol^{-1}). These transitions states prefer the same position as that of the isolated site on the *AC* and *AD* site-pairs, where they interact with O4 and O3 of the *A* site concurrently. The proton on the second site again bonds to O1 of the second site and bridges the 6-MR but confers no benefit. The Step C1 transition state on *AE*, however, is instead located in the larger CHA void and interacts simultaneously with the *A* and *E* sites. The nearby proton bonds to O4 of the *E* site and does not participate directly in the reaction; instead, the negativity of the AlO_4^- tetrahedron donates electrons to the positively charged transition state.

Table S2. Changes in effective ($\Delta\Delta G^{\neq}$) and intrinsic ($\Delta\Delta G_{act}$) free energy barriers for kinetically relevant Step S1 and Step C1.

Site	Second Site State	$\Delta\Delta G^{\neq}$ / kJ mol^{-1}		$\Delta\Delta G_{act}$ / kJ mol^{-1}
		Step S1	Step C1	Step C1
NNN	Proton	+1	+4	+5
	CH_3OH monomer	−4	−5	−10
	CH_3OH dimer	+5	−11	−18
NNNN	Proton	+1	+3	−3
	CH_3OH monomer	−3	−15	−2
	CH_3OH dimer	−6	−13	−28

S6. Effects of guest species orientation

Because adsorbates have many stable or metastable binding configurations on a single T-site in zeolites, a rigorous analysis of guest species location is necessary to determine the preferred orientation of adsorbates and transition states in zeolites. Moreover, DFT optimization of these adsorbates and transition states only identifies local minima for species, rather than global minima. This discrepancy between initial structures—which are often user-generated—and preferred structures can lead to inaccurate predictions of catalytic properties. For example, by merely rotating toluene within the intersection of MFI, a set of structures with an energy range of 45 kJ mol^{-1} was generated.[15] Such large shifts are not exclusive to large or loosely bound adsorbates; reorientation of adsorbed dimethyl ether (DME) produced structures with a similar range of energies (~40 kJ mol^{-1}).[15]

We repeated these systematic reorientations for the methanol dehydration intermediates and transition states investigated in this work. Previous work identified three different types of reorientations that could be performed on adsorbates in H-form zeolites: acid site reorientations for strongly bound guest species, spatial reorientations for weakly bound intermediates, and internal rotations for transition states.[15] Figure S7 shows examples of these reorientations in the context of the methanol dehydration intermediates and transition states investigated in this work. Acid site reorientations were performed for any species strongly interacting with the acid site via H-bonding or an incipient bond (e.g., CH_3OH*. Step S1 transition state, Step C1 transition state). Spatial reorientations were performed on molecules which were not strongly bound and rotated about the x-axis, y-axis (equivalent to the *b* vector of CHA), and z-axis (equivalent to the *c* vector) through their centers of mass. Finally, oxygenate species in transition states (CH_3OH and H_2O) were rotated about incipient bonds to evaluate different H-bonding configurations. Some states exhibit a combination of these interactions. For states where two interactions exist, each moiety was reoriented according to its interaction with the framework. The reactants for Step S2 (CH_3OH adsorbed near CH_3–Z), for example, has both a CH_3 covalently bound to the framework and physisorbed CH_3OH (Fig. S7b). The CH_3OH was rotated around x-, y-, and z-axes and the CH_3 around the Si-Al axis (O_t-Al-Si-O_a reorientation, Fig. S7a). Similarly, the Step C1 transition state forms H-bonds to O atoms of the conjugate base; the entire transition state was rotated around the Si-Al axis of the O H-bound to the H_2O (O_t-Al-Si-O_a) and the angle above this O altered (O_t-O_a-A_1-A_2), in addition to the internal reorientations shown in Figure S7c. In each case, an optimized structure was reoriented and each new structure re-optimized. Nonsensical structures where the guest species collided with the framework were discarded. The lowest energy configuration among these reoriented structures was shown for all structures in the main text for isolated sites.

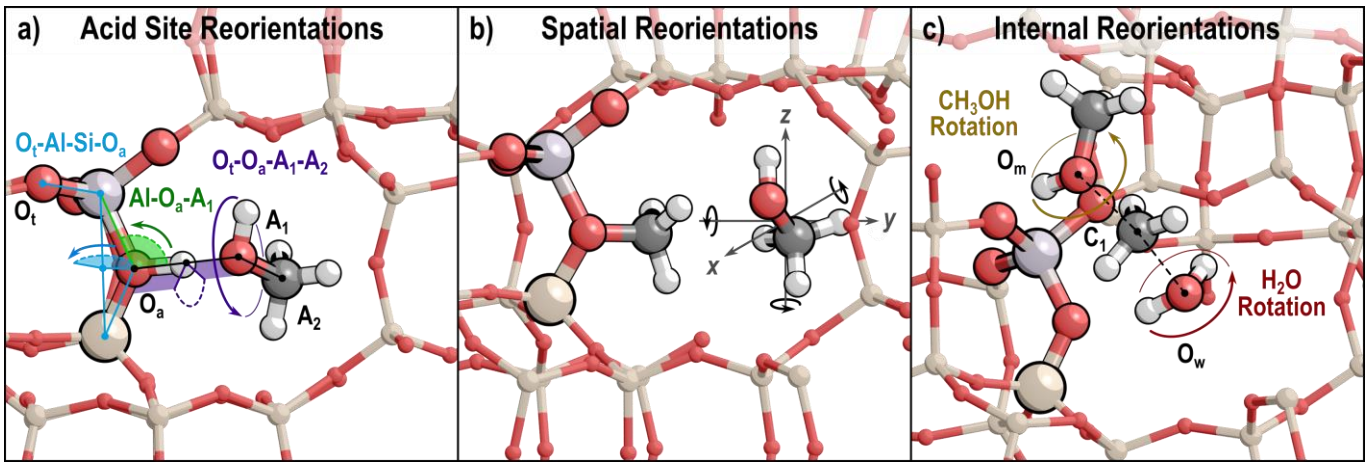

Figure S7. Three different types of reorientations performed for methanol dehydration adsorbates and intermediates: (a) acid site reorientations and (b) spatial reorientations, and (c) internal reorientations. (a) Acid site reorientations for a species interacting with O_a of the acid site consisted of rotations about the about the Al-Si axis of the two atoms bound to O_a (O_t-Al-Si-O_a), rotations about H-bonds to the acid site or O of the conjugate base (Ot-Oa-A_1-A_2), and alteration of the bond formed by the Al, O_a, and adsorbate atom (Al-O_a-A_1). (b) Spatial reorientations for adsorbates which were not strongly bound were rotated about the x-, y-, and z-axes through their centers of mass. (c) Oxygenate moieties in transition states were rotated around incipient bonds.

These reorientations produce structures with a range of energies in CHA, as reorientations for large adsorbates produced for arene methylations in MFI.[15] Optimized structures with identical connectivity and composition can have energy ranges > 40 kJ mol^{-1} (Fig. S8), which arise exclusively because of differences in the way guest species interact with the framework. Notably, Fig. S8 only shows energies for structures within 50 kJ mol^{-1} of the best identified structure; the energies of these species can vary by up to 200 kJ mol^{-1} on isolated sites in CHA. These reorientations identified 99 additional methanol monomer structures (CH_3OH-HZ) up to 9 kJ mol^{-1} more stable than optimized user-input structures. Such a decrease is smaller than that found in previous work for larger benzene adsorbates, for which these reorientations can identify structures as much as 40 kJ mol^{-1} lower in energy than input structures.[15] These results, however, are consistent with the small decreases found upon reorienting smaller oxygenate species—namely DME—for which there are smaller decreases in the best reoriented structures (<10 kJ mol^{-1}).[15] No one reorientation scheme for methanol monomers systematically identified more stable structures: on O1 and O2, altering the O_t-Al-Si-O_a angle resulted in the most stable structures, while on O3 and O4 altering the Al-O_a-A_1 angle identified the best structures. Similar insensitivity to specific reorientation scheme was found for methanol near CH_3Z, for which reorientations identified 170 additional structure but which also did not yield structures with energies more than 9 kJ mol^{-1} lower than their initial inputs. Notably, despite the energetic similarity between the best reoriented structures and their inputs, these reorientations still identify a number of nonideal structures, which can inform understanding and quantification of the favorable interactions within zeolite frameworks.

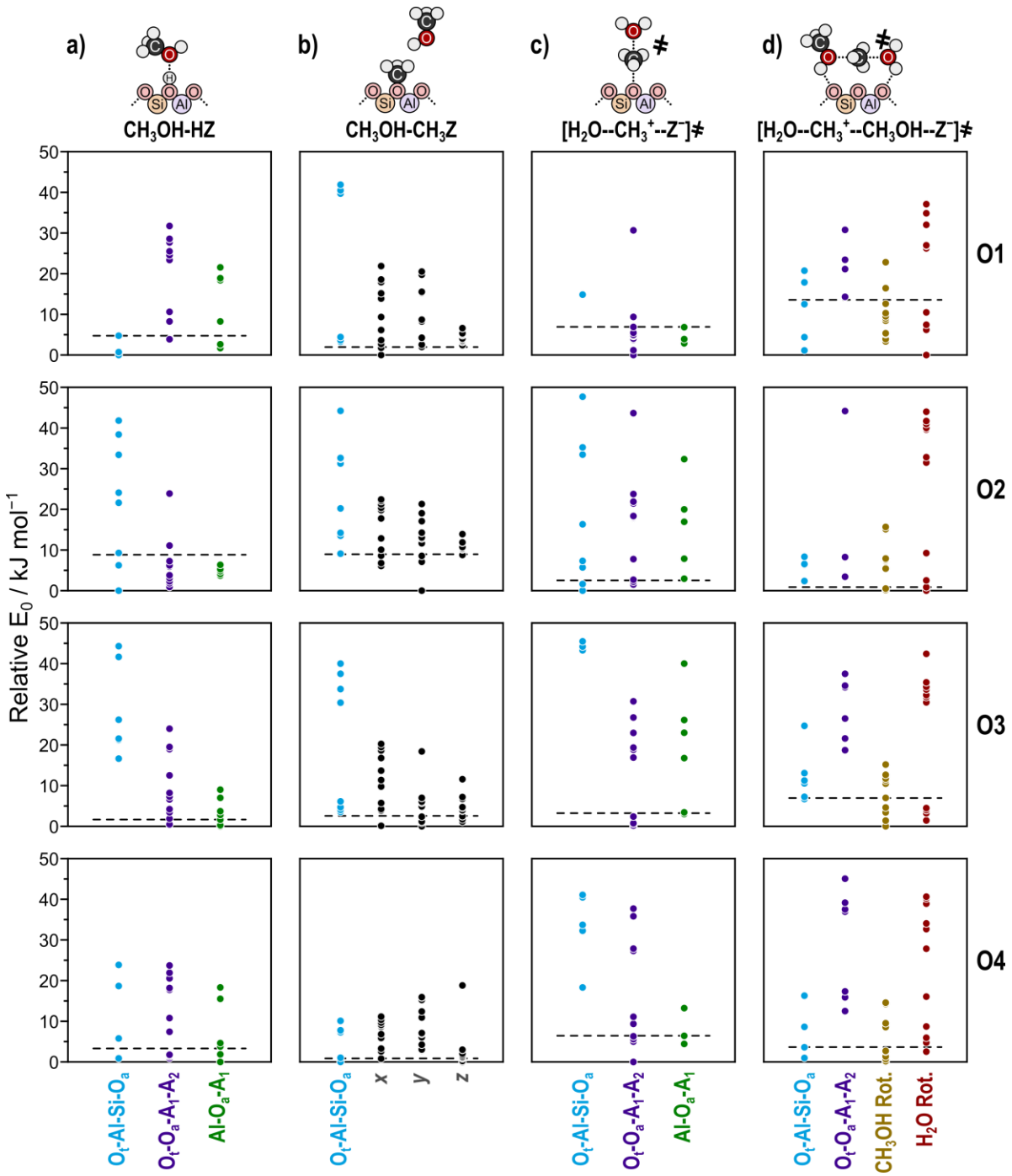

Figure S8. Effects of reorientations on the energies of (a) adsorbed methanol monomers (CH_3OH-HZ), (b) methanol adsorbed near a surface methyl group (CH_3OH-CH_3Z), (c) the transition state for the first step of the sequential mechanism (Step S1, $[H_2O\text{--}CH_3^+\text{--}Z^-]^{\neq}$), and (d) the transition state for the concerted mechanism (Step C1, $[H_2O\text{--}CH_3^+\text{--}CH_3OH\text{--}Z^-]^{\neq}$). Dots represent optimized structures after acid site reorientations (O_t-Al-Si-O_a, light blue; O_t-O_a-A_1-A_2, purple; Ot-Oa-A_1, green), spatial reorientations about the x-, y-, and z-axes (grey), and internal reorientations (CH_3OH rotation, yellow; H_2O rotation, red), while horizontal dashed lines represent initial structures. Energies relative to the best structure on each O atom for each state are shown in kJ mol^{-1}.

These reorientations are particularly critical for transition states, whose computational isolation is more costly and challenging than that for minima. Moreover, the transient structures which mediate this chemistry are extremely sensitive to the environments containing them and systematic reorientations help identify motifs which stabilize these transition states. These systematic reorientations of the Step S1 transition state produced 91 new structures with energy ranges of 100, 55, 207, and 205 kJ mol^{-1} on O1, O2, O3, and O4, respectively, but identified structures only up to 7 kJ mol^{-1} lower in energy than input structures. Concerted DME formation (Step C1) transition states form strong H-bonds to surface O atoms, but no bonds form or break with surface O atoms. As such, reorientation of this state included internal rotations of the H_2O and CH_3OH around the inchoate and cleaving bonds with the C of the methyl group between them (Figure S7c). We also rotate the entire transition state around the H-bond it forms to the conjugate base of the site on which the reaction occurs, without breaking the H-bond. Reorientation of the larger Step C1 transition state results in larger reductions in energy from the input structure than Step S1—14 kJ mol^{-1} for the state where the H_2O is H-bonding to O1—consistent with larger improvements upon reorientation of larger adsorbates in previous work.[15]

While these reorientations did not regularly identify structures with energies more than 10 kJ mol^{-1} lower than user-input structures, they aid in the determination of structural motifs which stabilize these intermediates and transition states. Such analysis increases the likelihood of identifying the structures of these guest species which are preferred in experiments but which are not directly observable. The reflection of these complex realities is a critical aspect of modeling reactions using DFT.

S7. Thermochemical cycles showing energy required to move transition states and add proximal site

Thermochemical cycles can be used to reflect the difference between two identical transition states in different locations and with different site proximities. Here, we calculate the energy difference between these configurations for the Step S1 transition state on an isolated site and on the *AC* (NNN) and *AD* (NNNN) site-pairs.

Moving the surface methylation transition state from a position above O3 to O4 increases the overall barrier by 13 kJ mol^{-1} to 148 kJ mol^{-1} (Figure S12). The addition of a nearby proton on O1 in the NNN position decreases the barrier for this transition state (which is the preferred configuration with a nearby bare proton) by 7 kJ mol^{-1}. This overall barrier of 141 kJ mol^{-1} is still higher than that for methylation of an isolated site at O3 (135 kJ mol^{-1}) but the nearby proton does offer some stabilization of the transition state relative to the methanol monomer. The addition of a coadsorbed methanol on the unreacting site, however, increases this stabilizing effect, reducing the barrier by an additional 10 kJ mol^{-1}.

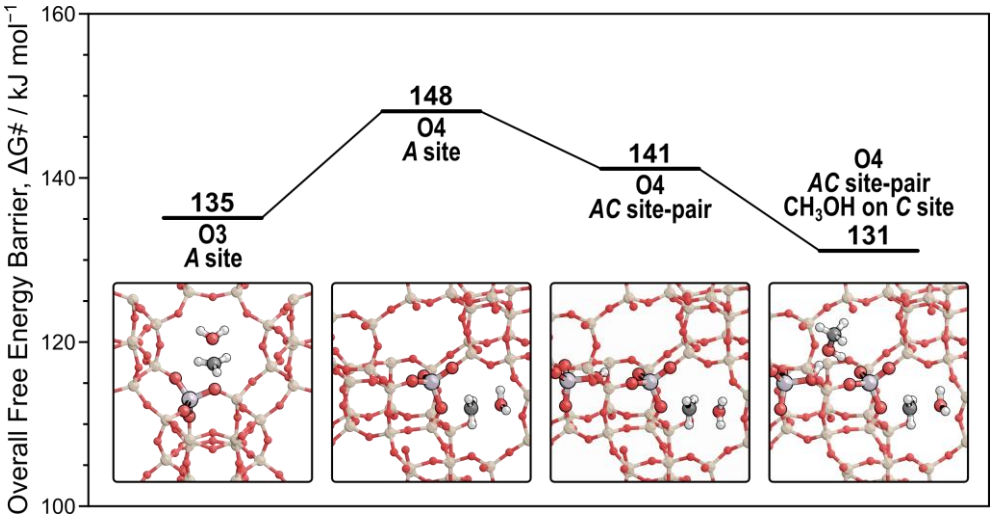

Figure S9. Thermochemical cycle showing the energy to move the Step S1 transition state from O3 to O4, add a nearby Brønsted acid site (in the *C* position), and adsorb a methanol to the nearby *C* site.

The benefit of the nearby proton on the transition state where O4 is methylated with a site at the NNNN position is greater than that for the NNN site (Figure S13). The overall barrier for the best Step S1 transition state on the NNNN pair (O4 methylation) is still 1 kJ mol^{-1} higher than the best Step S1 transition state on an isolated site (O3 methylation). Additional coadsorbed methanol further reduces this barrier to 132 kJ mol^{-1}, similar to the overall barrier of surface methylation on the NNN site-pair with coadsorbed methanol (131 kJ mol^{-1}). This similarity reflects the consistency for nearby coadsorbed methanol to stabilized these transition states, regardless of the effects of the nearby bare proton.

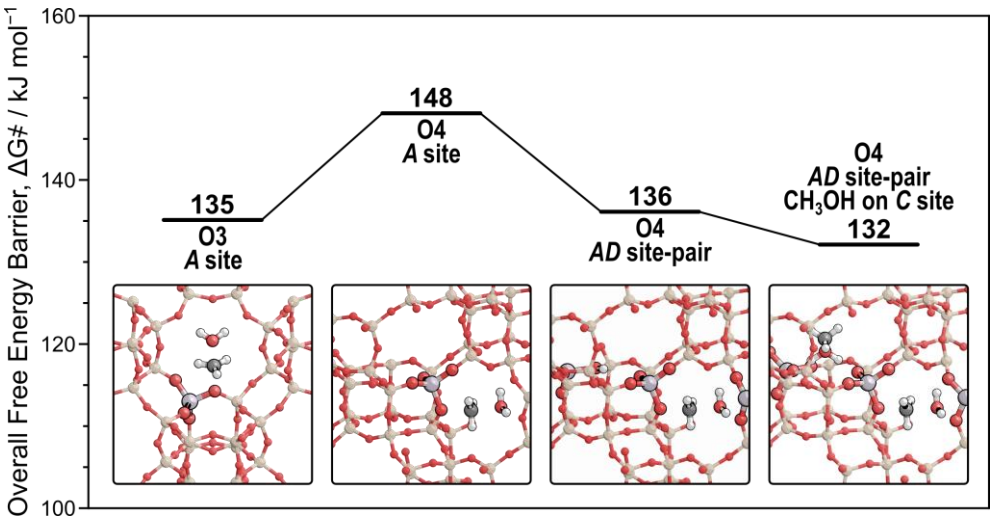

Figure S10. Thermochemical cycle showing the energy to move the Step S1 transition state from O3 to O4, add a nearby Brønsted acid site (in the *D* position), and adsorb a methanol to the nearby *D* site.

S8. Additional methanol dehydration structures and energies on paired sites

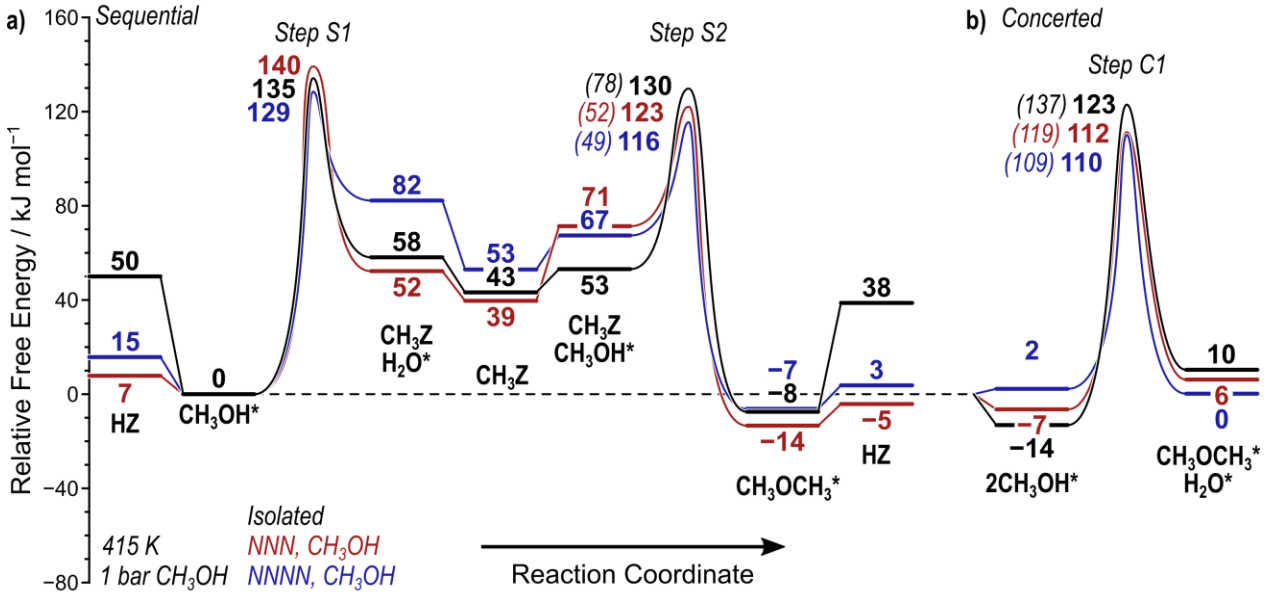

Figure S11. Reaction coordinate diagram for (a) sequential and (b) concerted methanol dehydration on isolated sites (black), the NNN site-pair with a CH_3OH dimer on the second site (red) and the NNNN site-pair with a CH_3OH dimer at the second site (blue). Energies are shown relative to a methanol monomer on the reacting site and a dimer on the unreacting site. Intrinsic barriers are shown for Steps S2 and Step C1 in parentheses.

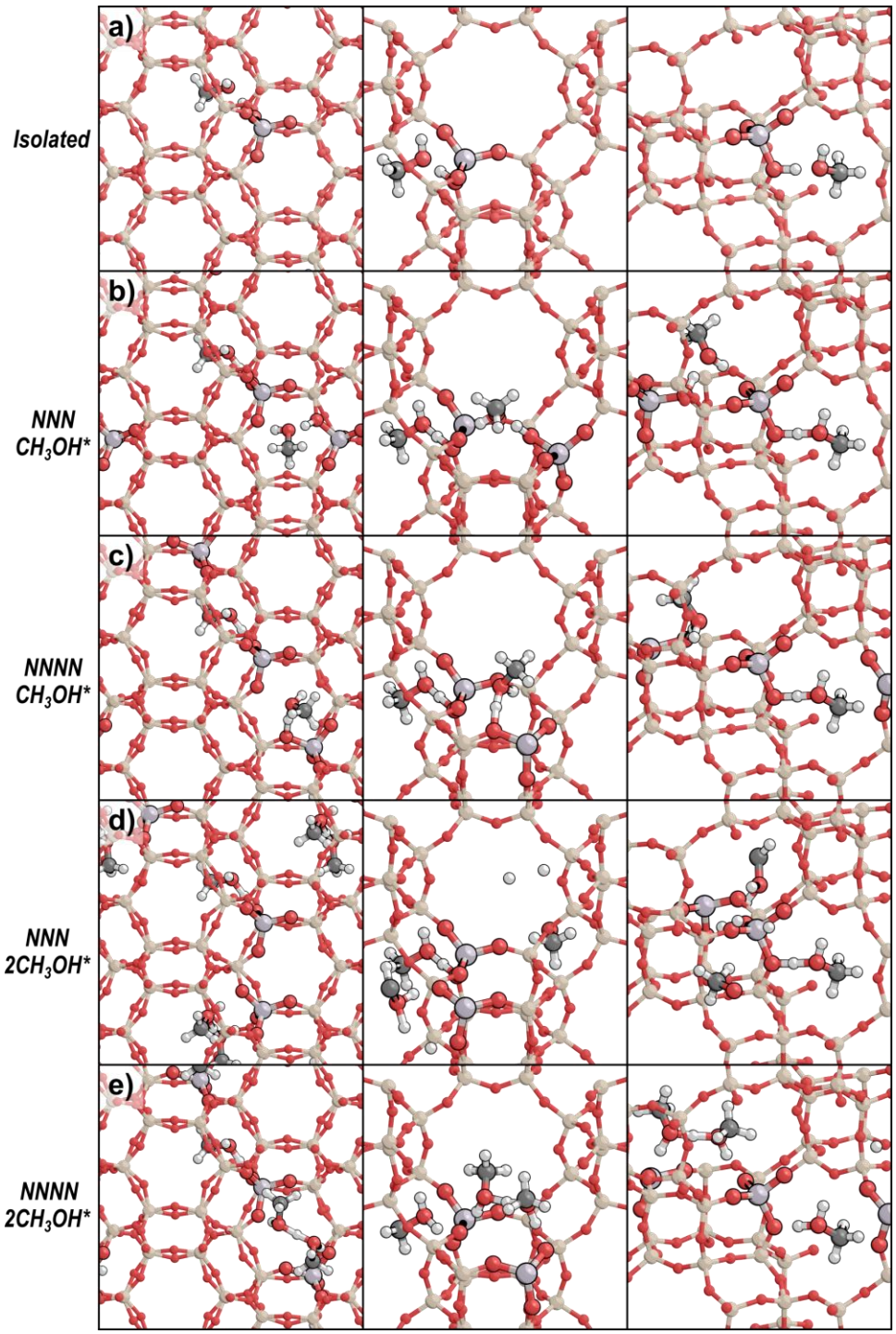

Figure S12. Methanol monomers on (a) isolated sites, (b) the NNN site-pair with a monomer on the second site, (c) the NNNN site-pair with a monomer on the second site, (d) the NNN site-pair with a dimer on the second site, and (e) the NNNN site-pair with a dimer on the second site. Views are shown down the *c*-vector (left), emphasizing 8-MR(2,3) (middle), and emphasizing 8-MR(2,4) (right).

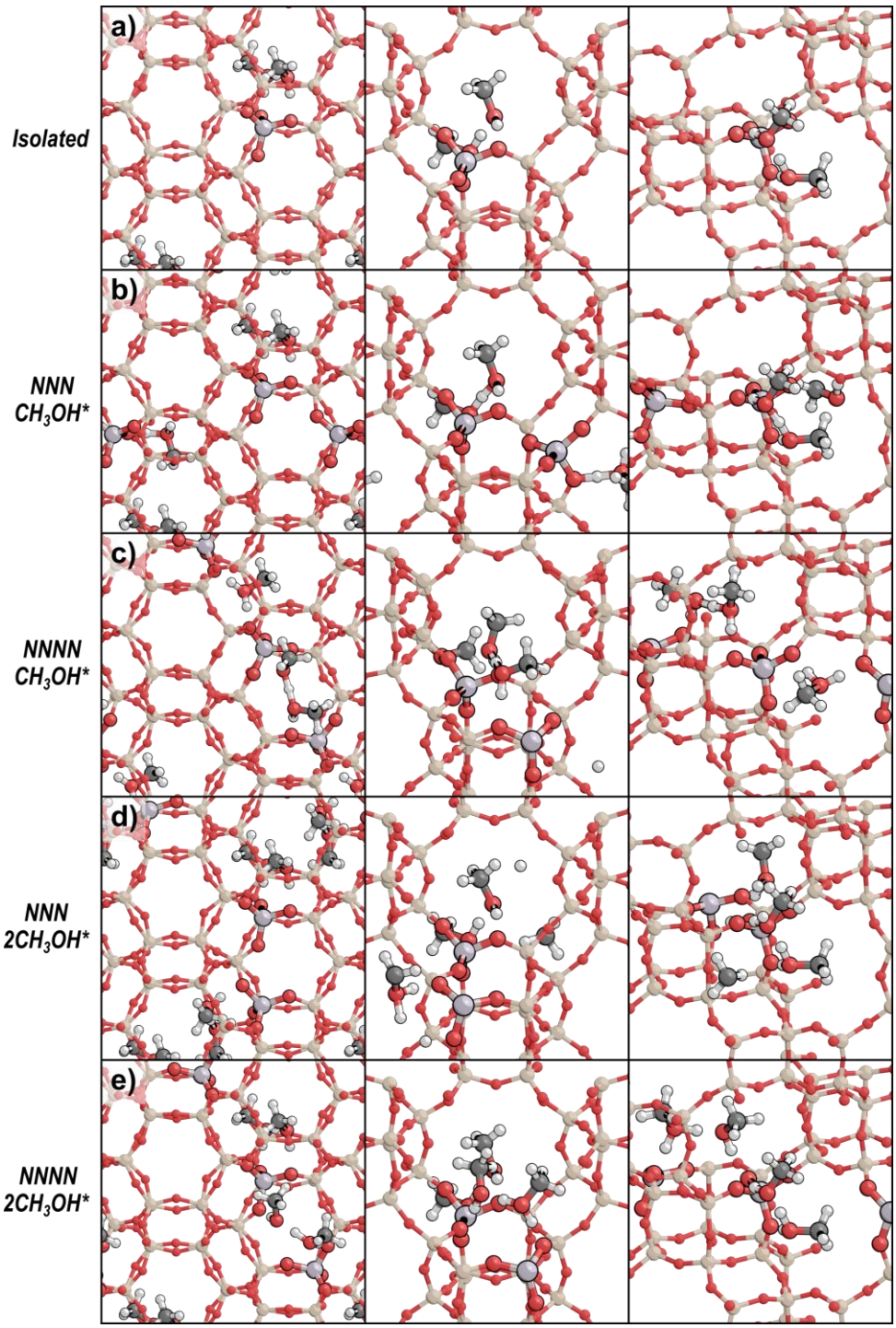

Figure S13. Methanol dimers on (a) isolated sites, (b) the NNN site-pair with a monomer on the second site, (c) the NNNN site-pair with a monomer on the second site, (d) the NNN site-pair with a dimer on the second site, and (e) the NNNN site-pair with a dimer on the second site. Views are shown down the *c*-vector (left), emphasizing 8-MR(2,3) (middle), and emphasizing 8-MR(2,4) (right).

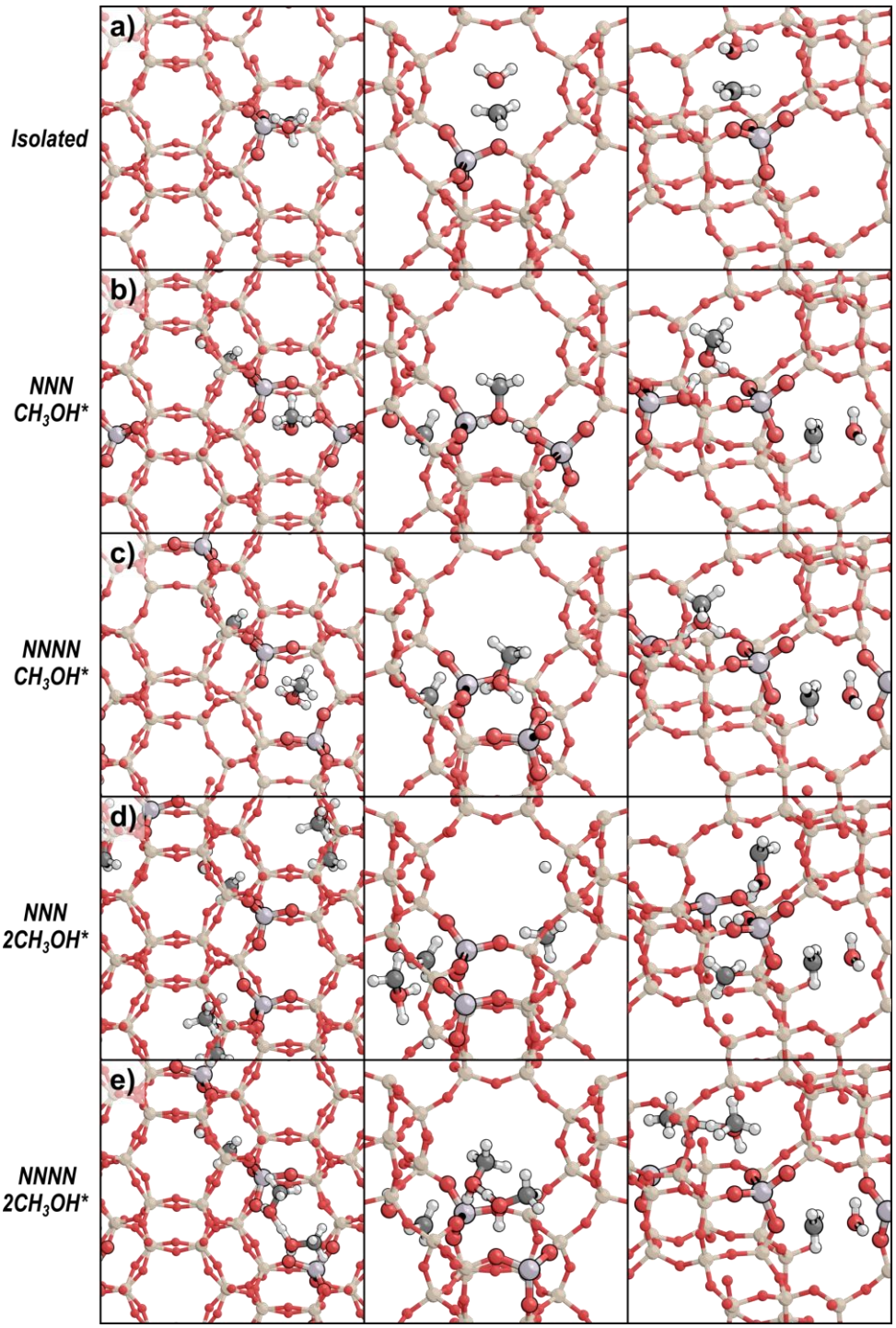

Figure S14. Methanol Step S1 transition state on (a) isolated sites, (b) the NNN site-pair with a monomer on the second site, (c) the NNNN site-pair with a monomer on the second site, (d) the NNN site-pair with a dimer on the second site, and (e) the NNNN site-pair with a dimer on the second site. Views are shown down the *c*-vector (left), emphasizing 8-MR(2,3) (middle), and emphasizing 8-MR(2,4) (right).

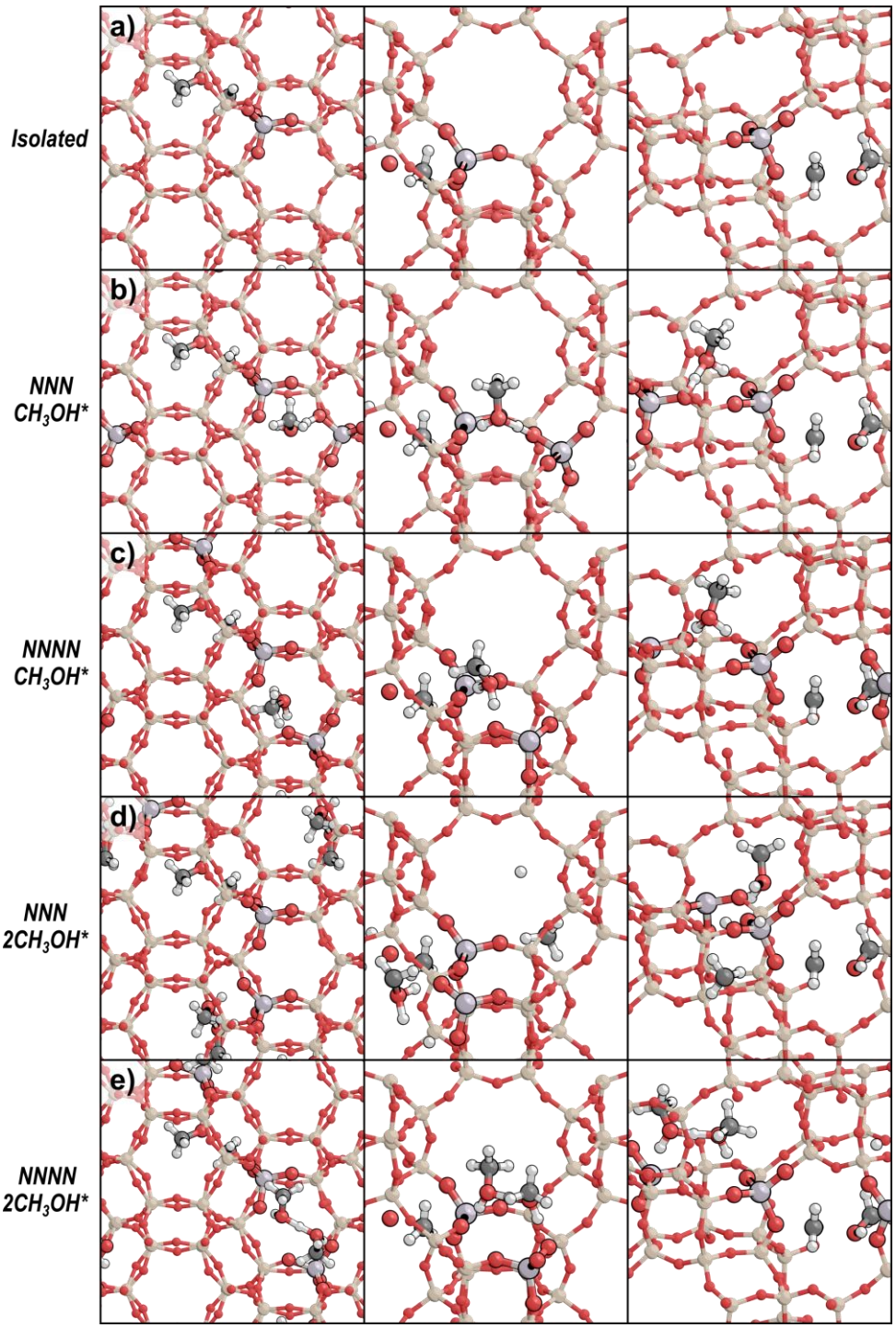

Figure S15. Methanol Step S2 transition state on (a) isolated sites, (b) the NNN site-pair with a monomer on the second site, (c) the NNNN site-pair with a monomer on the second site, (d) the NNN site-pair with a dimer on the second site, and (e) the NNNN site-pair with a dimer on the second site. Views are shown down the *c*-vector (left), emphasizing 8-MR(2,3) (middle), and emphasizing 8-MR(2,4) (right).

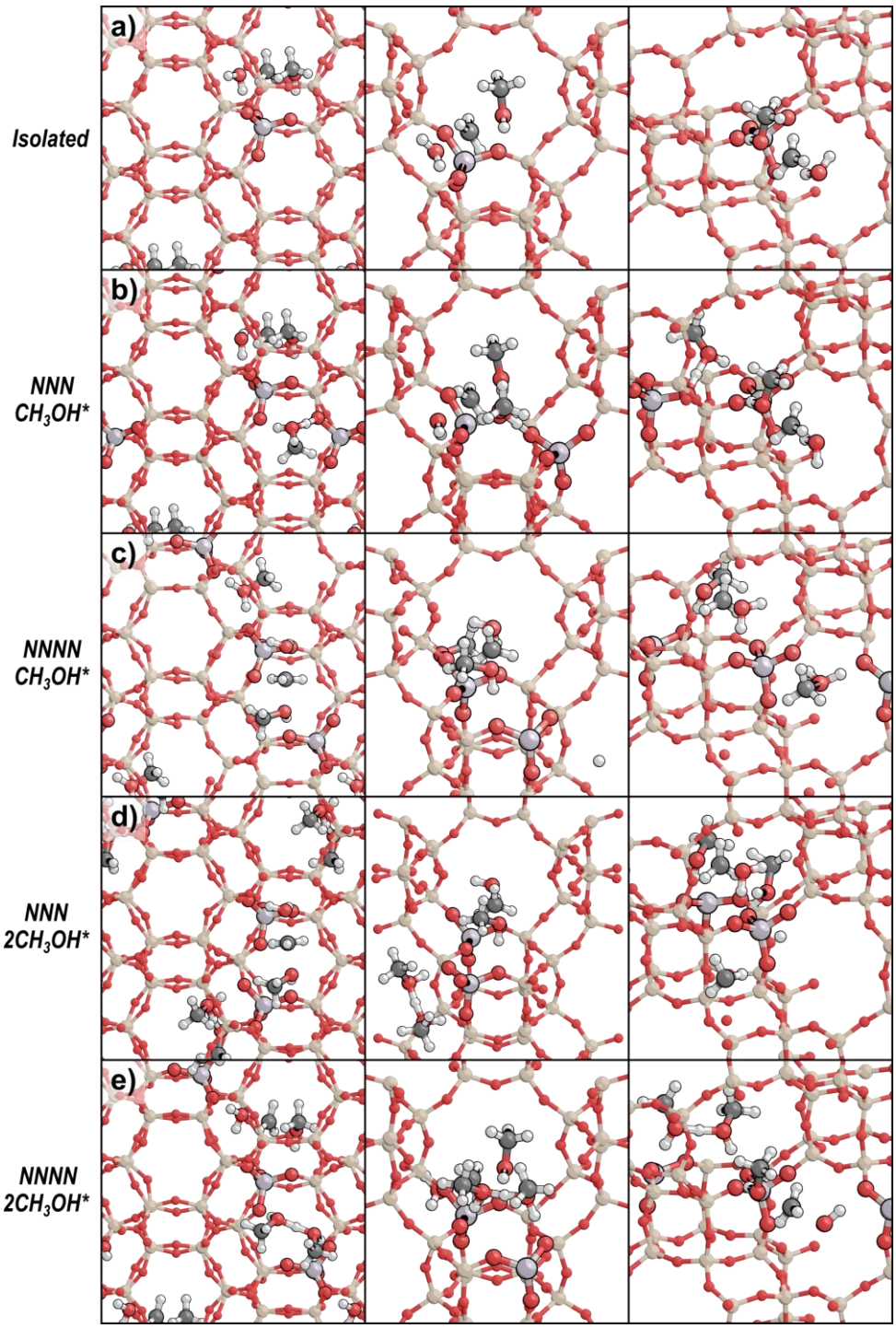

Figure S16. Methanol Step C1 transition state on (a) isolated sites, (b) the NNN site-pair with a monomer on the second site, (c) the NNNN site-pair with a monomer on the second site, (d) the NNN site-pair with a dimer on the second site, and (e) the NNNN site-pair with a dimer on the second site. Views are shown down the *c*-vector (left), emphasizing 8-MR(2,3) (middle), and emphasizing 8-MR(2,4) (right).

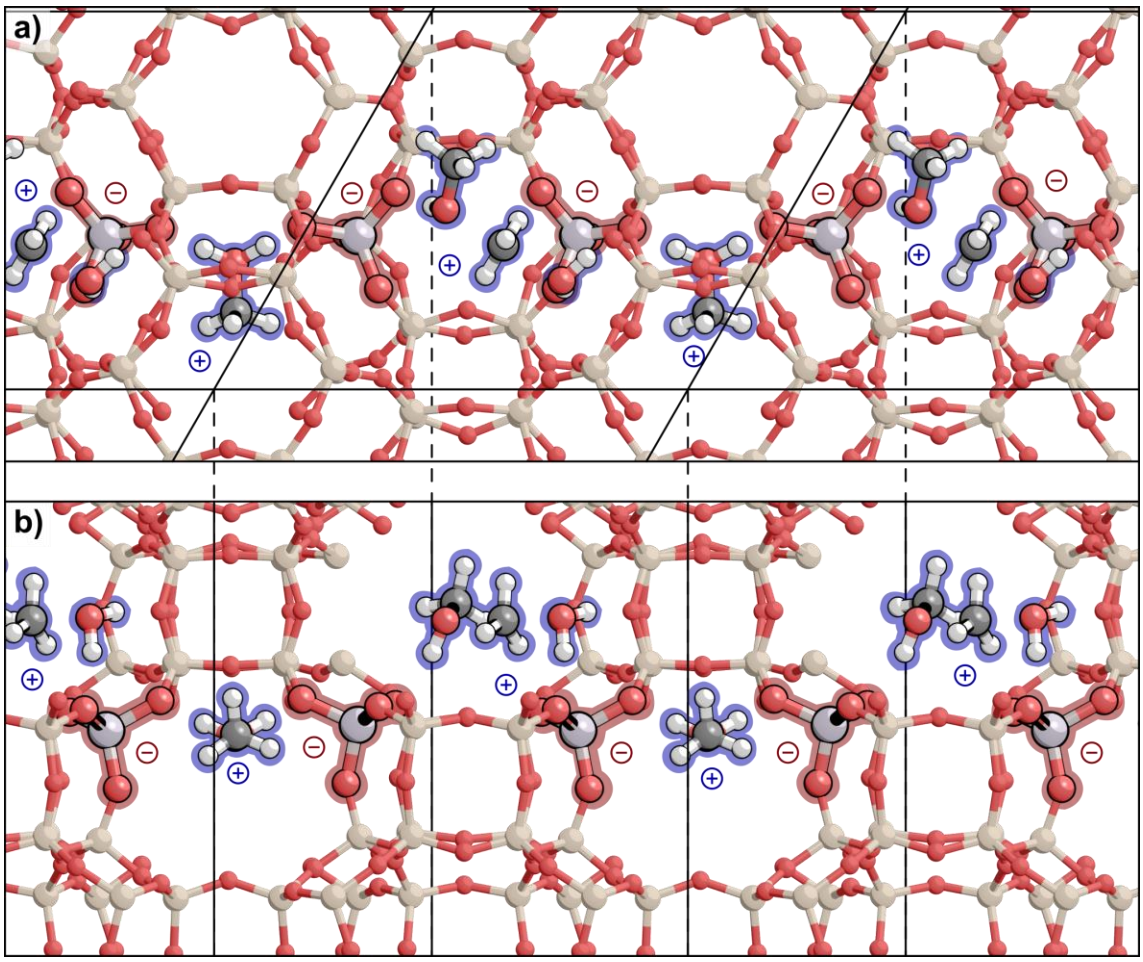

Figure S17. The Step C1 transition state on the NNNN site-pair with a methanol on the second site shown (a) along the c-vector of the CHA unit cell, with the unit cell outlined with a black solid line and (b) in the plane formed by the *a*- and *c*-vectors with corresponding boundaries of the unit cell indicated by solid lines from part (a). Cationic species (Step C1 transition state and protonated methanol monomer) are highlighted in blue and conjugate anions are highlighted in red.

S9. Methanol dehydration rate equation derivation

The possible pathways for methanol dehydration to DME have been well-established in prior studies.[16,24,48–53] Methanol dehydration can occur by concerted or sequential routes (Scheme 1, main text). Sequential methanol dehydration proceeds via formation of a surface methyl group, which can methylate a second methanol molecule. Concerted methanol dehydration occurs via an adsorbed methanol dimer where simultaneous dehydration and methylation liberate DME and water. Previously we showed that the concerted mechanism dominates at isolated H^+ sites in small-pore CHA zeolites[24,26] and can be generally described by:

$$r_{DME,C1} = \frac{\sum_{i=2}^{6} k_{DME,i} K_i P_M^i}{\sum_{i=1}^{6} K_i P_M^i} \quad \text{(S18)}$$

where $k_{DME,i}$ is the rate constant for concerted DME formation, K_i is a lumped equilibrium constant to adsorb i methanol molecules ranging in size from 1-6 methanols, and P_M is the pressure of methanol. DFT identified that the preferred concerted transition state is comprised of 3 CH_3OH molecules with coverages at these conditions (415 K, 0.05-50 kPa CH_3OH) ranging from 1–5 CH_3OH, but largely remained at 2–4 CH_3OH per H^+. Therefore, Eq. S18 can be simplified to

$$r_{DME,C1} = \frac{k_{DME,3} K_3 P_M^3}{K_2 P_M^2 + K_3 P_M^3 + K_4 P_M^4} = \frac{k_{DME,3} K_3 P_M}{K_2 + K_3 P_M + K_4 P_M^2} \quad \text{(S19)}$$

which is of the same form as Eq. 1 in the main text.

S10. DFT analysis of ethanol dehydration on isolated and paired sites

Ethanol dehydration to DEE can proceed by nearly identical pathways to those observed for methanol dehydration to DME—via sequential or concerted routes. As such, these pathways follow the same mechanism shown in Scheme 1 (main text) but with an ethyl group instead of a methyl. Therefore, we use the same notation to denote relevant elementary steps in DEE formation for surface ethylation (Step S1), ethanol ethylation from a surface ethyl (Step S2), and concerted DEE formation (Step C1). We calculate the structures for the transition states for each of these steps on an isolated site and on NNN and NNNN site-pairs with 1–2 ethanol molecules adsorbed to the unreacting site.

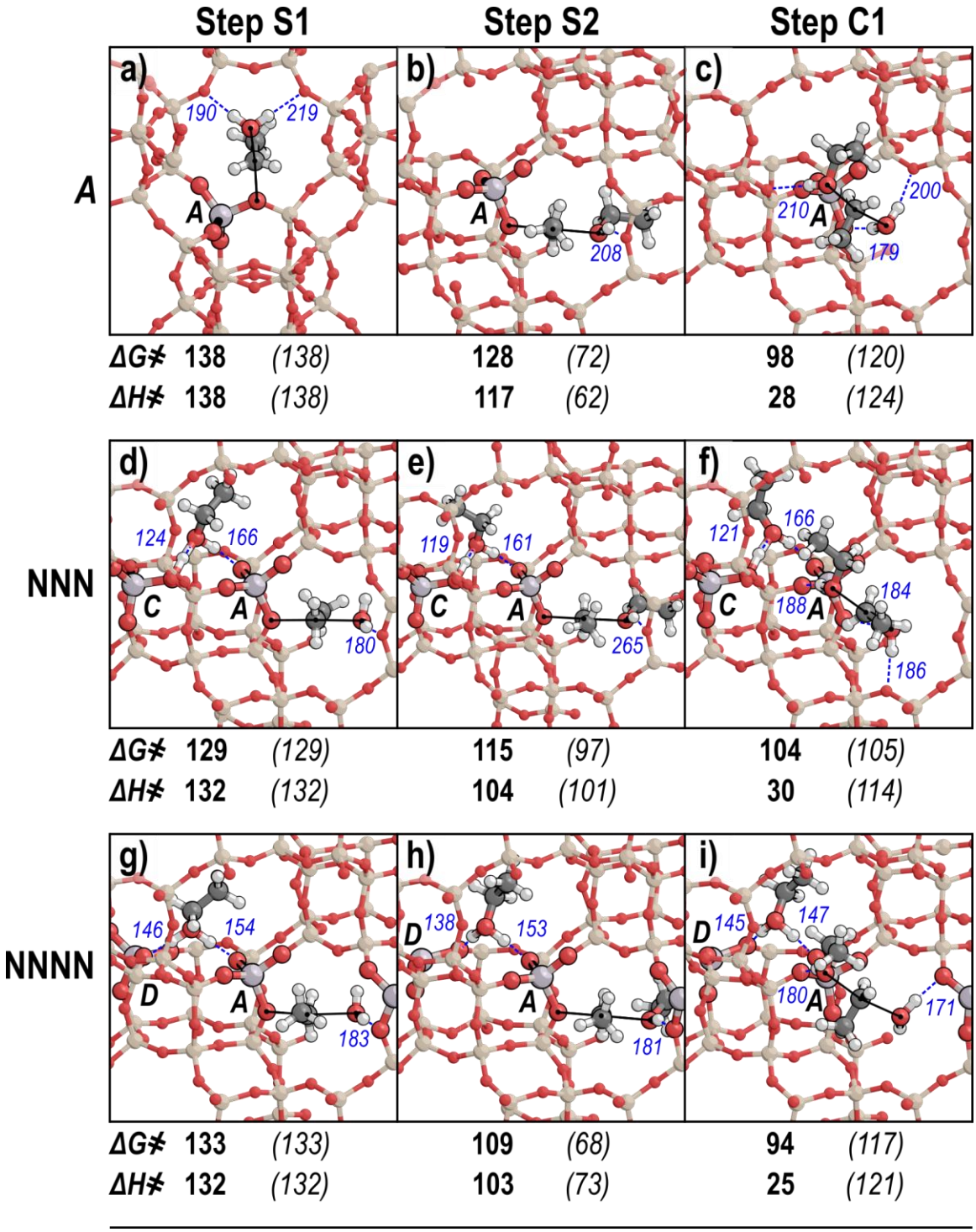

Figure S18. The most favorable transition state structures found for ethanol dehydration in CHA for Step S1 (a,d,g), Step S2 (b,e,h), and Step C1 (c,f,i) for isolated (a-c) acid sites and site-pairs in the NNN (d-f), and NNNN arrangements (g-i). Their effective free energy (415 K, 1 bar) and enthalpy barriers ($\Delta G^{\neq}$ and $\Delta H^{\neq}$) and their intrinsic barriers (ΔG_{act} and ΔH_{act} in parenthesis and italicized) are shown in kJ mol^{-1}. Solid black lines indicate incipient and breaking bonds while blue dashed lines indicate H-bonds, whose lengths are labeled in pm.

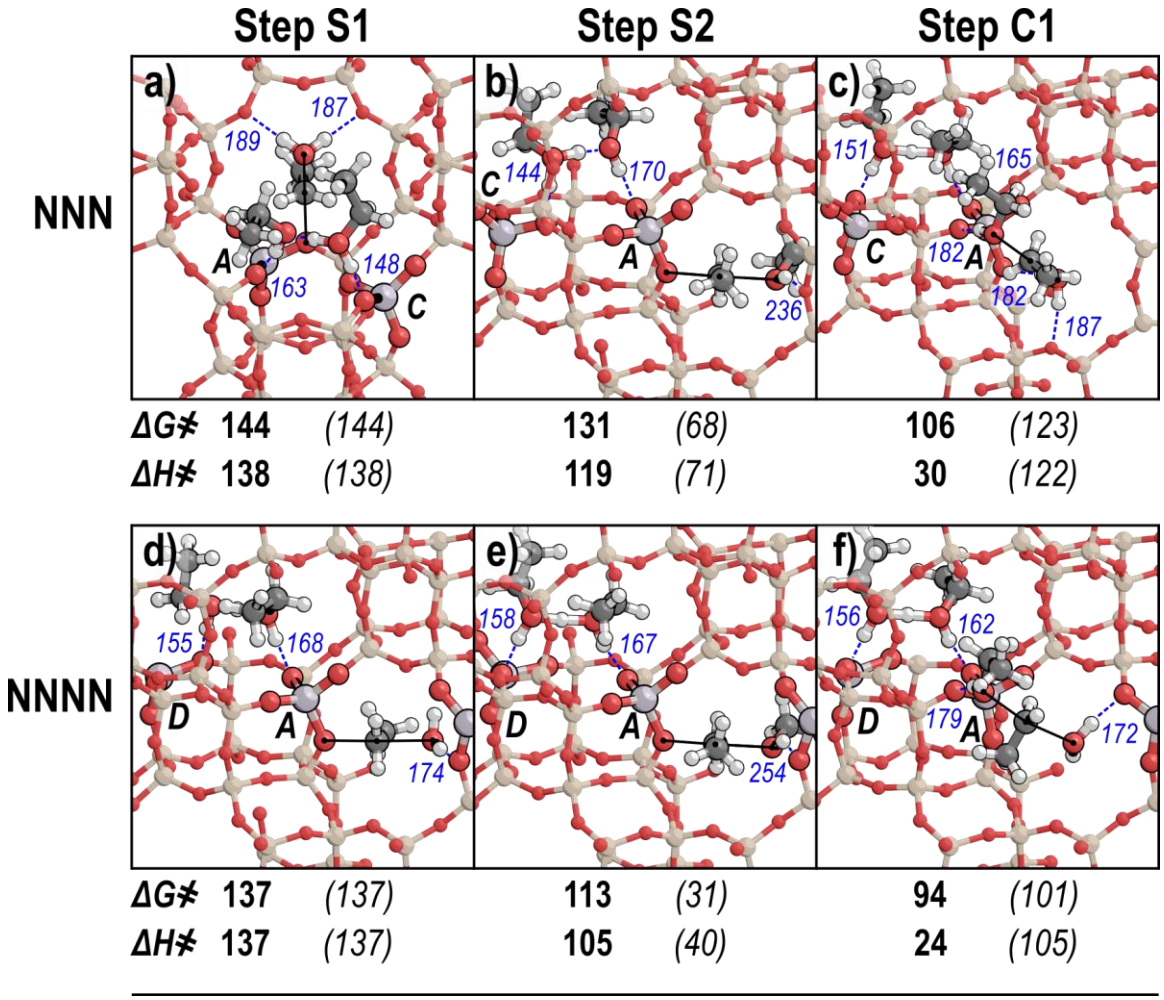

Figure S19. The most favorable transition state structures found for ethanol dehydration in CHA for Step S1 (a,d,g), Step S2 (b,e,h), and Step C1 (c,f,i) for isolated (a-c) acid sites and site-pairs in the NNN (d-f), and NNNN arrangements (g-i). Their effective free energy (415 K, 1 bar) and enthalpy barriers ($\Delta G^{\neq}$ and $\Delta H^{\neq}$) and their intrinsic barriers (ΔG_{act} and ΔH_{act} in parenthesis and italicized) are shown in kJ mol^{-1}. Solid black lines indicate incipient and breaking bonds while blue dashed lines indicate H-bonds, whose lengths are labeled in pm.

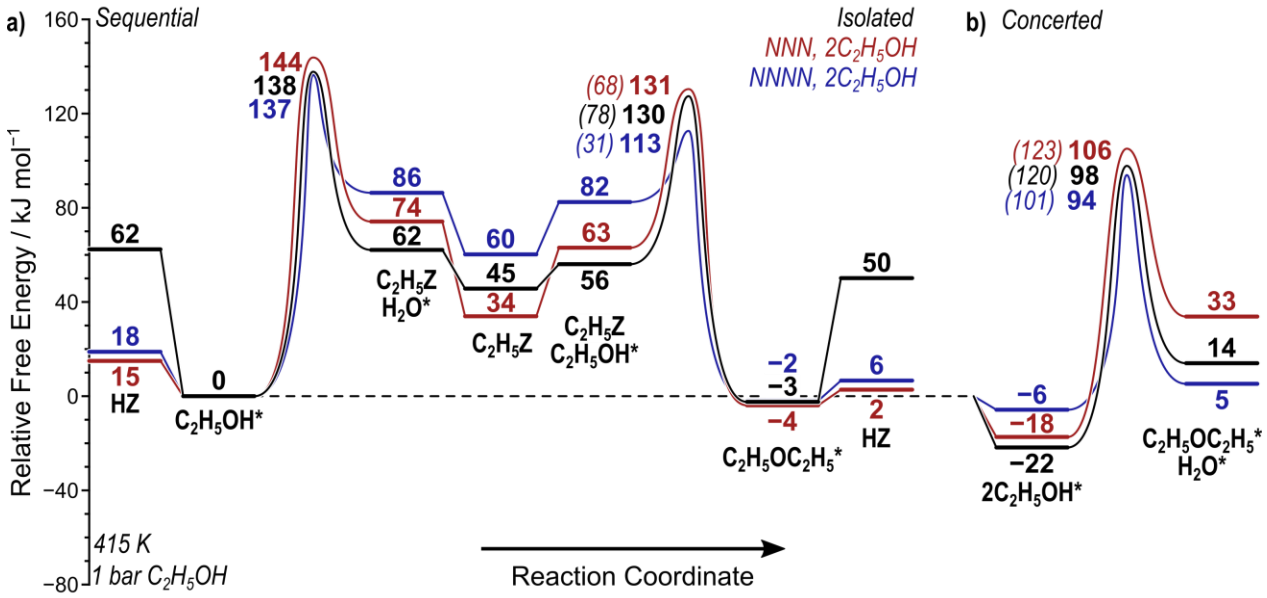

Figure S20. Reaction coordinate diagram for (a) sequential and (b) concerted methanol dehydration on isolated sites (black), the NNN site-pair with a C_2H_5OH dimer at the second acid site (red), and the NNNN site-pair with a C_2H_5OH dimer at the second site (blue). Free energies (415 K, 1 bar) are shown relative to a methanol monomer on all sites. Intrinsic barriers are shown for Steps S2 and Step C1 in parentheses.

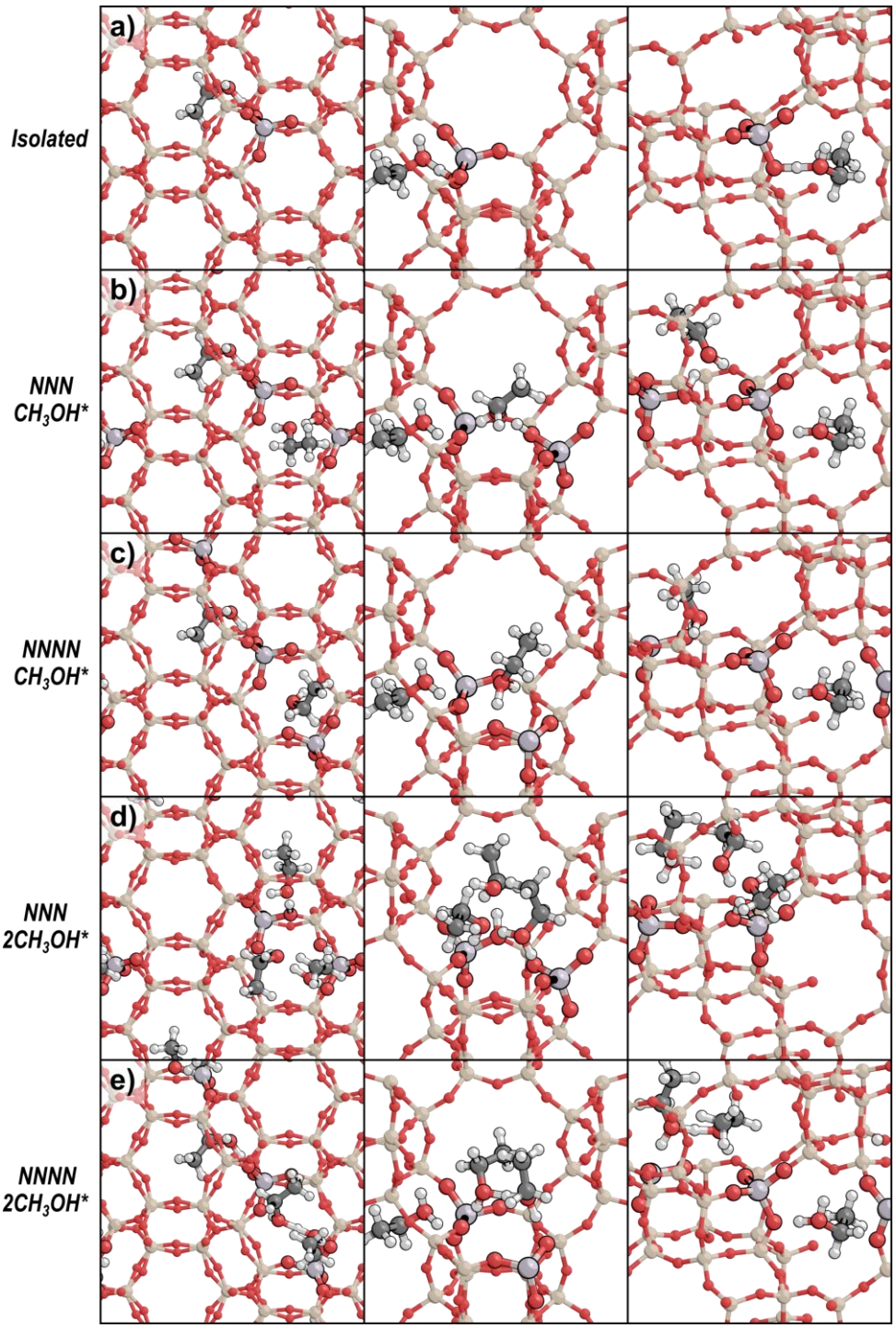

Figure S21. Ethanol monomers on (a) isolated sites, (b) the NNN site-pair with a monomer on the second site, (c) the NNNN site-pair with a monomer on the second site, (d) the NNN site-pair with a dimer on the second site, and (e) the NNNN site-pair with a dimer on the second site. Views are shown down the *c*-vector (left), emphasizing 8-MR(2,3) (middle), and emphasizing 8-MR(2,4) (right).

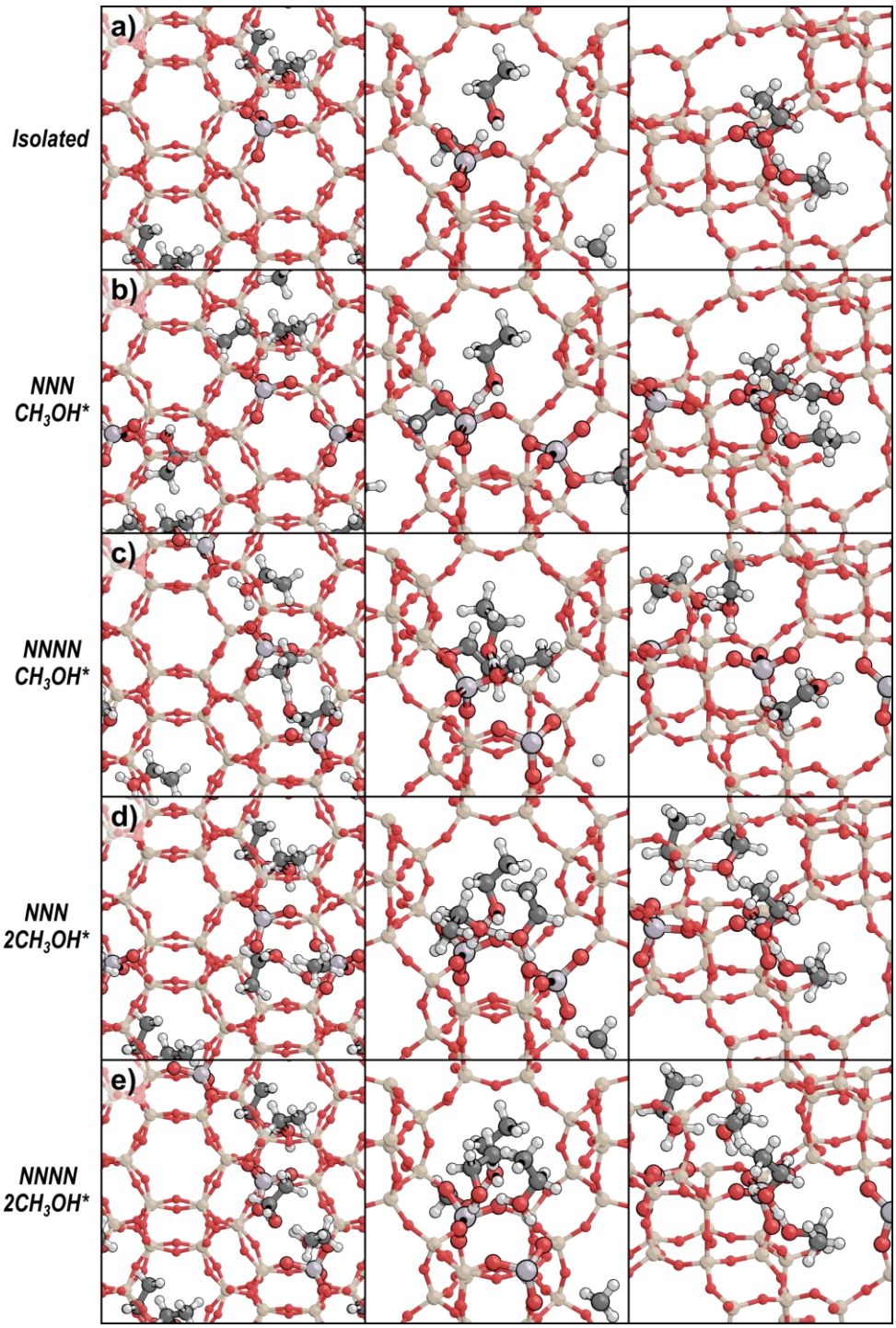

Figure S22. Ethanol dimers on (a) isolated sites, (b) the NNN site-pair with a monomer on the second site, (c) the NNNN site-pair with a monomer on the second site, (d) the NNN site-pair with a dimer on the second site, and (e) the NNNN site-pair with a dimer on the second site. Views are shown down the *c*-vector (left), emphasizing 8-MR(2,3) (middle), and emphasizing 8-MR(2,4) (right).

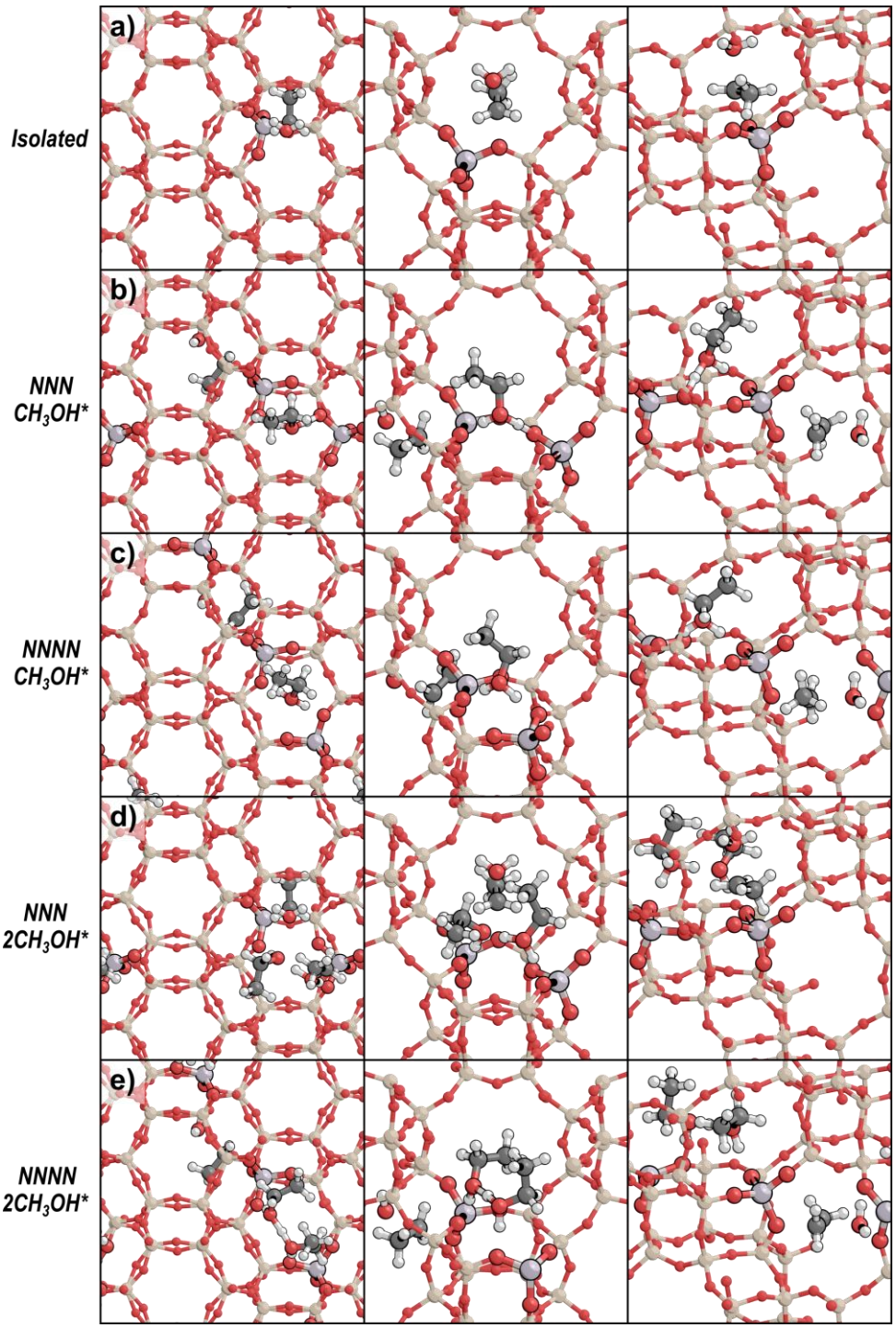

Figure S23. Ethanol Step S1 transition state on (a) isolated sites, (b) the NNN site-pair with a monomer on the second site, (c) the NNNN site-pair with a monomer on the second site, (d) the NNN site-pair with a dimer on the second site, and (e) the NNNN site-pair with a dimer on the second site. Views are shown down the *c*-vector (left), emphasizing 8-MR(2,3) (middle), and emphasizing 8-MR(2,4) (right).

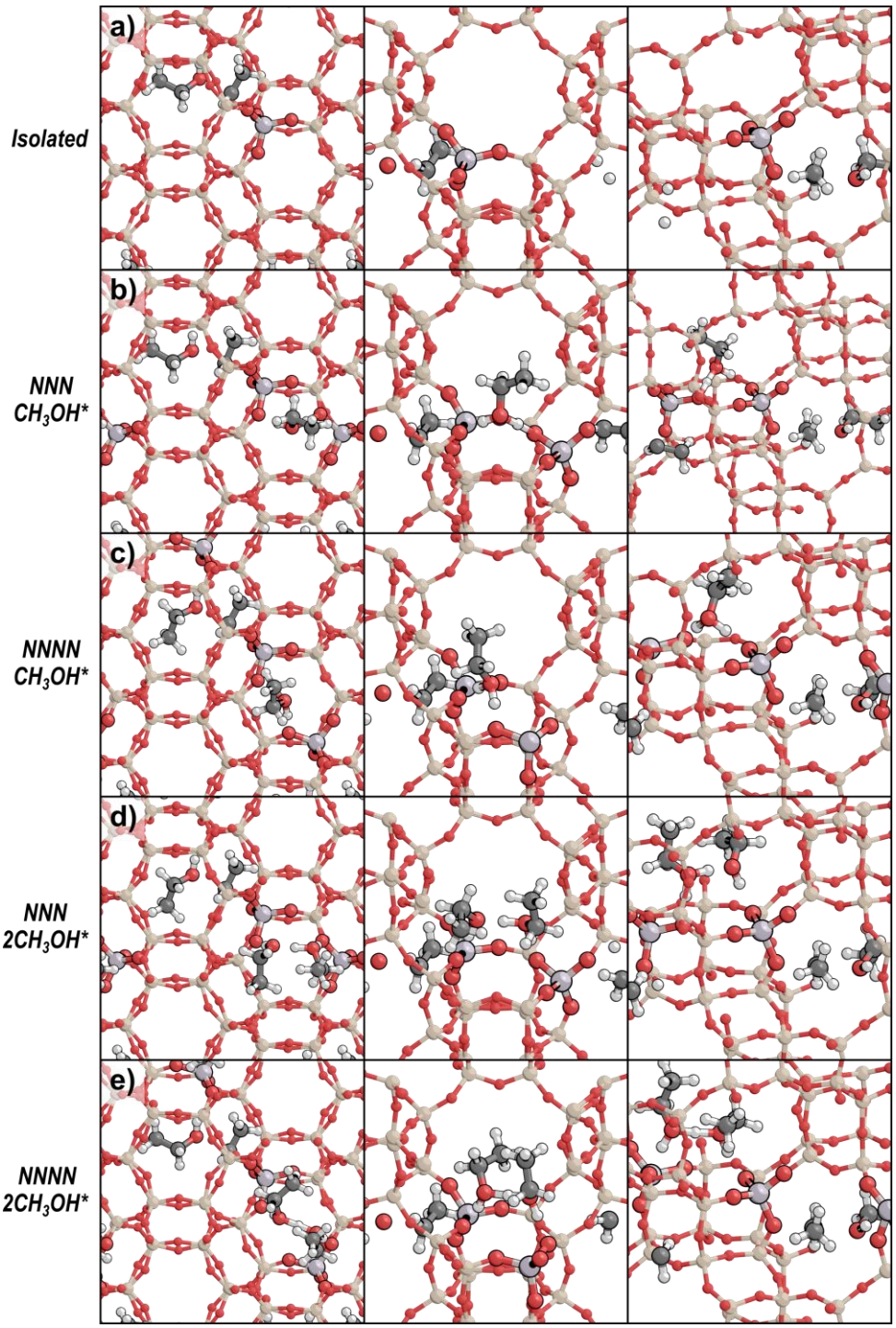

Figure S24. Ethanol Step S2 transition state on (a) isolated sites, (b) the NNN site-pair with a monomer on the second site, (c) the NNNN site-pair with a monomer on the second site, (d) the NNN site-pair with a dimer on the second site, and (e) the NNNN site-pair with a dimer on the second site. Views are shown down the *c*-vector (left), emphasizing 8-MR(2,3) (middle), and emphasizing 8-MR(2,4) (right).

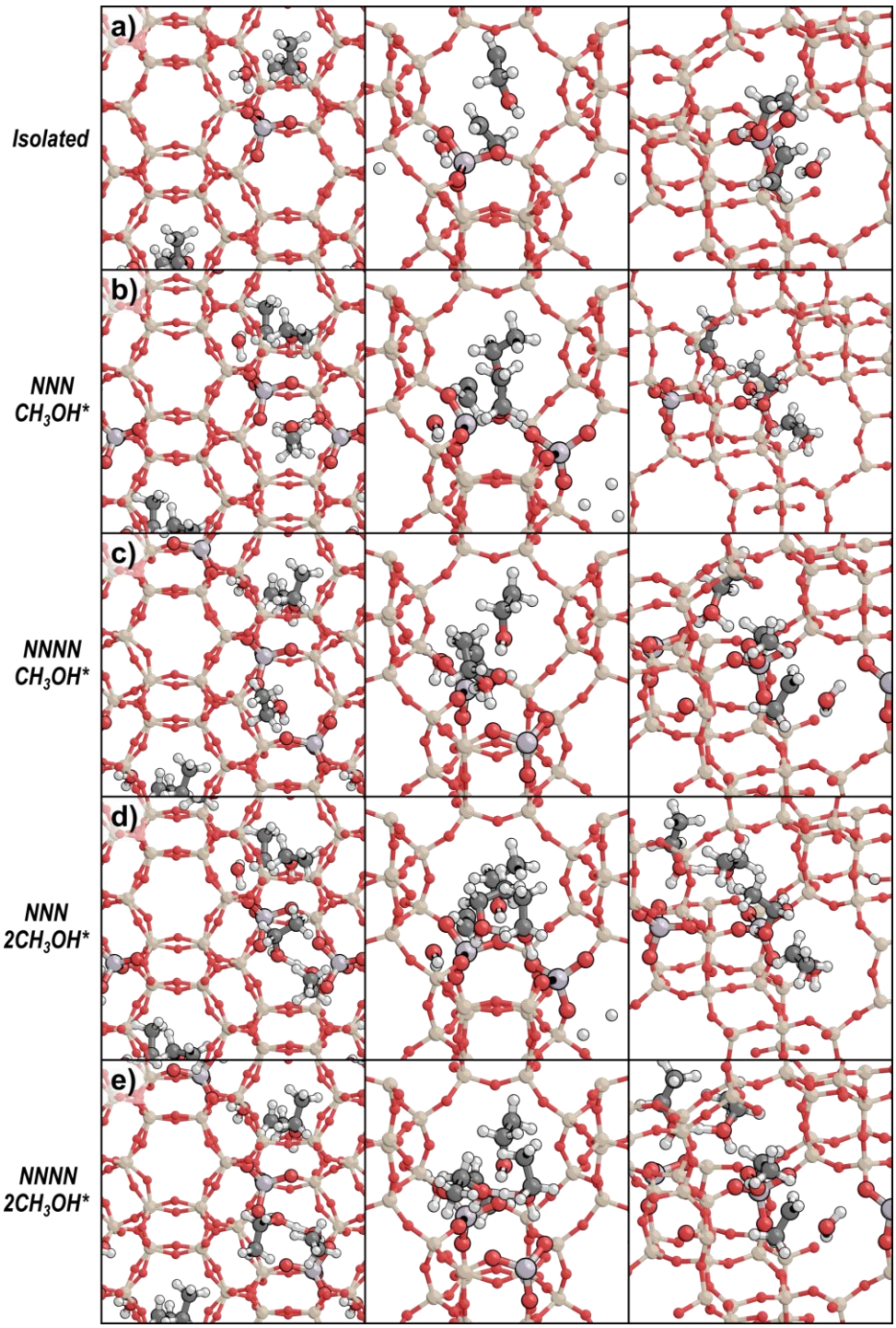

Figure S25. Ethanol Step C1 transition state on (a) isolated sites, (b) the NNN site-pair with a monomer on the second site, (c) the NNNN site-pair with a monomer on the second site, (d) the NNN site-pair with a dimer on the second site, and (e) the NNNN site-pair with a dimer on the second site. Views are shown down the *c*-vector (left), emphasizing 8-MR(2,3) (middle), and emphasizing 8-MR(2,4) (right).

S11. Ethanol dehydration kinetics in CHA zeolites with systematically altered site pairing

Three H-CHA samples were studied here spanning Al_{pair}/Al_{tot} values from 0–0.44 to probe the influence of proximity on ethanol dehydration catalysis (Table S1, Section S2). Ethanol dehydration site-time yields (STY, per H^+) to form both diethyl ether (DEE, Figure 8, main text) and ethene (EY, Fig. S26a) were quantified on H-CHA zeolites at 415 K and C_2H_5OH pressures between 0.05–69 kPa. EY was observed at all C_2H_5OH pressures tested at this temperature in H-CHA, in contrast to H-MFI and H-FER zeolites at 409 K,[54] but consistent with H-MOR zeolites at 409 K,[54] which likely occurs because 8-MR side pockets stabilize EY formation transition states.

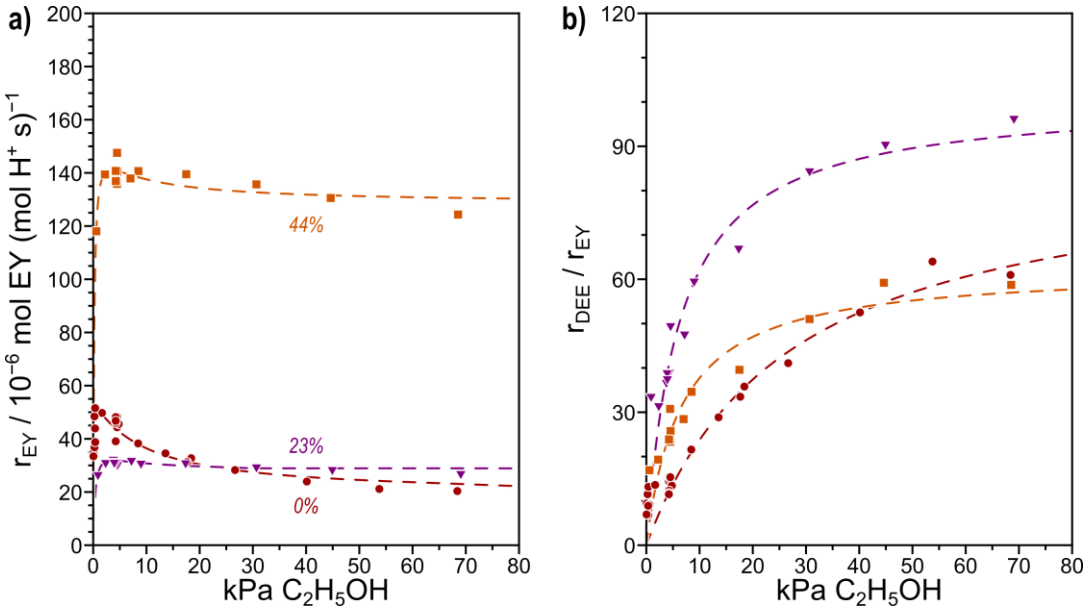

Figure S26. (a) Turnover rates (415 K, per H^+) for EY formation in H-CHA with 0% (red), 22% (purple), and 44% (orange) of Al in paired configurations. Dashed lines represent fits to Equation S27 (b) The ratio of DEE and EY formation rates in H-CHA with 0% (red), 22% (purple), and 44% (orange) of Al in paired configurations. Dashed lines represent fits to Equation S28.

As discussed in Section S10, ethanol dehydration to DEE follows the same elementary steps as methanol dehydration but with a different alkyl group. DEE formation, however, is not inhibited at high pressures (>20 kPa C_2H_5OH, 415 K) in H-CHA regardless of the fraction of Al in paired configurations and only possesses first- and zero-order regimes (Fig. 8, main text). These kinetic data indicate that at all conditions analyzed for ethanol dehydration in this work, transition states form from most abundant surface intermediates (MASI) with an equal or lesser number of alcohol constituents, in contrast with methanol dehydration, for which methanol must desorb at high pressures to form TS with fewer constituent alcohols than the MASI.[16] Prior work has identified concerted DEE formation as the kinetically relevant step and ethanol monomers and protonated dimer complexes as potential MASI. If this step for DEE formation (Step C1) is the sole kinetically relevant step, then the site-time yield (STY, per H^+) is described by

$$r_{DEE} = \frac{k_{DEE}K_M K_D P_E^2}{1+K_M P_E+K_M K_D P_E^2} \cong \frac{k_{DEE}K_D P_E}{1+K_D P_E} \quad \text{(S23)}$$

where K_M and K_D are the equilibrium constants for ethanol monomer and dimer formation, k_{DEE} is the rate constant for concerted DEE formation, and P_E is the pressure of ethanol. This can be expressed in terms of first- and zero-order rate coefficients as in Eq. 2 in the main text:

$$r_{DEE} = \frac{k_{first} P_E}{1 + \frac{k_{first}}{k_{zero}} P_E} \quad \text{(S24)}$$

where $k_{first} = k_{DEE}K_D$ and $k_{zero} = k_{DEE}$. Because the Brønsted acid sites are covered by alcohol monomers, dimers, and larger complexes at conditions relevant to catalysis for ethanol dehydration (e.g., on POM[55]), $K_M P_E \gg 1$ and $K_M K_D P_E^2 \gg 1$ and the rate equation can be simplified, consistent with prior kinetic measurements on zeolites[54] and fitted values of K_M with large errors (Table S3). This equation describes the STY of DEE formation on all H-CHA samples analyzed in this work (Figure 8, main text).

Table S3. Regressed ethanol dehydration rate and equilibrium constants on H-CHA zeolites.

Zeolite Name	K_M / kPa^{-1}	K_D / kPa^{-1}	k_{DEE} / 10^{-4}[a]	$k_{EY,m}$ / 10^{-5}[a]	$k_{EY,d}$ / 10^{-5}[a]
H-CHA(0.44)[b]	5.1 ± 3.6	0.19 ± 0.05	80 ± 7	16 ± 1	24 ± 1
H-CHA(0.23)[b]	2.5 ± 0.7	0.22 ± 0.06	28 ± 2	3.9 ± 0.2	6.2 ± 0.1
H-CHA(0)[b]	20 ± 10	0.11 ± 0.07	17 ± 4	5.6 ± 0.5	2.1 ± 0.6
H^+_{iso}[c]	17.2	0.13	9.6	3.4	0.3
H^+_{pair}[c]	indeterminate	0.31	153.2	25.9	25.0
Pair/iso ratio[c]	--	2.3	16.0	7.7	72.7

[a]units [=] mol (mol H^+)$^{-1}$ s^{-1}
[b]Regressed in Athena Visual Studio separately to the data sets on each sample using Equations S23 and S27
[c]Determined from linear fit to 0% and 100% pairing (Fig. 8 inset, main text).

Rate expressions for EY formation developed in the literature reflect kinetically relevant unimolecular dehydration steps from the ethanol monomer species to form either ethene directly[56] or to form a surface-bound ethyl that subsequently forms ethene in kinetically irrelevant steps,[54] the latter of which is kinetically indistinguishable from the direct pathway. The formation rate of EY assuming unimolecular dehydration—either direct or sequential—is described by a similar equation

$$r_{EY,m} = \frac{k_{EY,m} K_M P_E}{1 + K_M P_E + K_M K_D P_E^2} \quad \text{(S25)}$$

where $k_{EY,m}$ is the rate constant for unimolecular EY formation. Assuming ethene is formed solely via unimolecular routes, the ratio r_{DEE}/r_{EY} is

$$\frac{r_{DEE}}{r_{EY}} = \frac{k_{DEE} K_D}{k_{EY,m}} P_E \quad \text{(S26)}$$

where $k_{DEE}K_D$ has been defined above, and $k_{EY,m}$ reflects the free energy of the ethene formation transition state relative to the adsorbed ethanol monomer species. Eq. S26 predicts that the r_{DEE}/r_{EY} ratio is linear in P_E, but instead the DEE/EY ratio (Fig. S26b) shows a non-linear dependence that has been previously ascribed to the

kinetic relevance of multiple parallel pathways to form either DEE or EY in kinetic measurements on polyoxometalate clusters.[55]

The apparent non-linear dependence of r_{DEE}/r_{EY} on P_E is primarily a consequence of the high-pressure kinetic dependence of the EY STY on P_E, which approaches a zero-order regime (Fig. S26a), whereas rate expressions based on monomolecular ethene formation steps would predict a limiting −1 order dependence on P_E when surfaces are saturated with ethanol-ethanol dimers. This zero-order limiting behavior was also observed by Chiang and Bhan on H-MOR,[54] who took this as evidence that H^+ confined within 8-MR side pockets were unable to stabilize ethanol-ethanol dimer species at $P_E < 6$ kPa, leading to rate expressions with two terms for dehydration in the 8-MR and 12-MR of MOR. This explanation is plausible within MOR, where certain T-sites may be embedded within confining side pockets and constrain reactive intermediates within them, but in CHA zeolites, every T-site (only one crystallographically unique T-site) is accessible within the less-confined CHA cage (~0.7 nm largest included sphere [57]). Alternatively, a spectating alcohol could stabilize the dehydration transition state for EY formation, as described for 1-propanol dehydration rates (per H^+) to form propylene in H-MFI zeolites (413–443 K, 0.075–4 kPa 1-propanol).[58] This leads to rate expressions for EY formation that are zero-order at high P_E:

$$r_{EY} = \frac{k_{EY,m}K_M P_E + k_{EY,d}K_M K_D P_E^2}{1 + K_M P_E + K_M K_{dimer} P_E^2} \quad \text{(S27)}$$

where $k_{EY,d}$ reflects the free energy of the ethene formation transition state, with one co-adsorbed ethanol molecule, referenced to the ethanol-ethanol dimer. Eq. S27 provides reasonable fits to the dependence of both r_{EY} (Fig. S26a) and r_{DEE}/r_{EY} (Fig. S26b) on P_E, when Eq. S23 and Eq. S23 are fit to the data in Figure 8 (main text) and Figure S26, to give values of k_{DEE}, $k_{DEE}K_D$, $k_{EY,m}$, and $k_{EY,d}$ that can be compared among samples with different Al_{pair}/Al_{total} values (Table S3). The inclusion of a bimolecular EY formation transition state yields a new equation describing the ratio of EY formation and DEE formation rates:

$$\frac{r_{DEE}}{r_{EY}} = \frac{k_{DEE}K_M K_D P_E^2}{k_{EY,m}K_M P_E + k_{EY,d}K_M K_D P_E^2} \quad \text{(S28)}$$

which agrees well with experimentally measured r_{DEE}/r_{EY} ratios (Fig. S26b).

S12. Surface methylation with varying Si:Al

Al were added to locations that were identified as critical influencers of acid strength—as measured by deprotonation energy (DPE) and NH_3 binding energy—in prior work (Figure S27).[20] Al were systematically added to each of these positions without violating Löwenstein's rule, initially from the best methanol monomer and Step S1 transition state on O3 with only one Al in the unit cell (Figure S28). Subsequent Al additions were made to the structures with the two highest barriers and the three lowest barriers and five other structures with intermediate barriers of interest (namely sites sharing 6-MR). This process was repeated until 5 Al were incorporated into the unit cell (Si:Al ratio of 6.2).

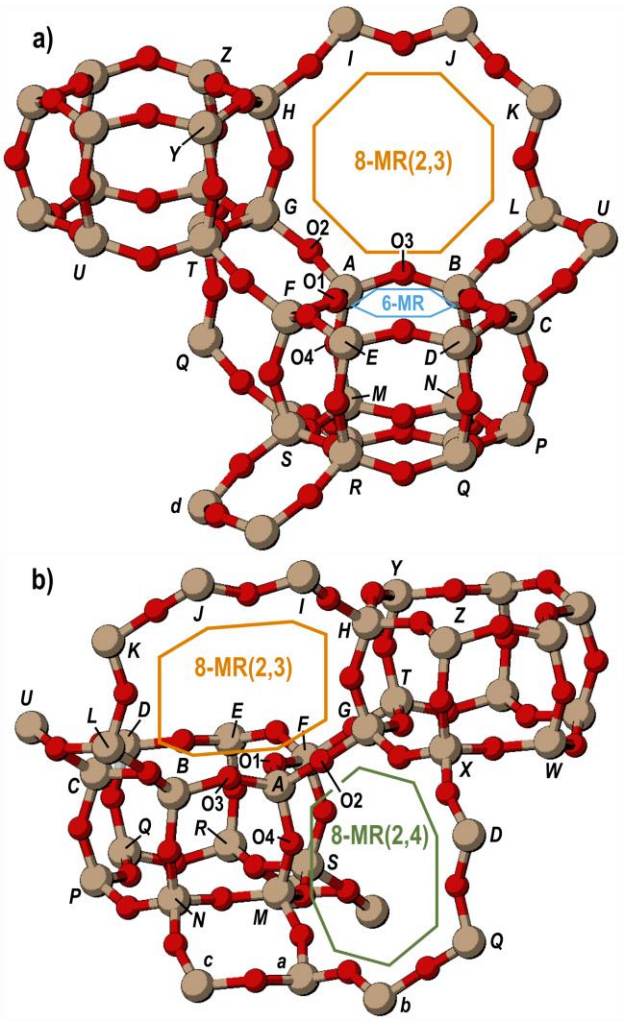

Figure S27. Locations at which additional Al were added to decrease Si:Al ratio shown (a) emphasizing the 6-MR adjacent to the *A* site and (b) emphasizing the 8-MR(2,4) adjacent to the *A* site. One Al remained at the *A* site in all calculations and Al were added at other sites to vary the Si:Al ratio except in positions violating Löwenstein's rule. Adapted from previous work.[20]

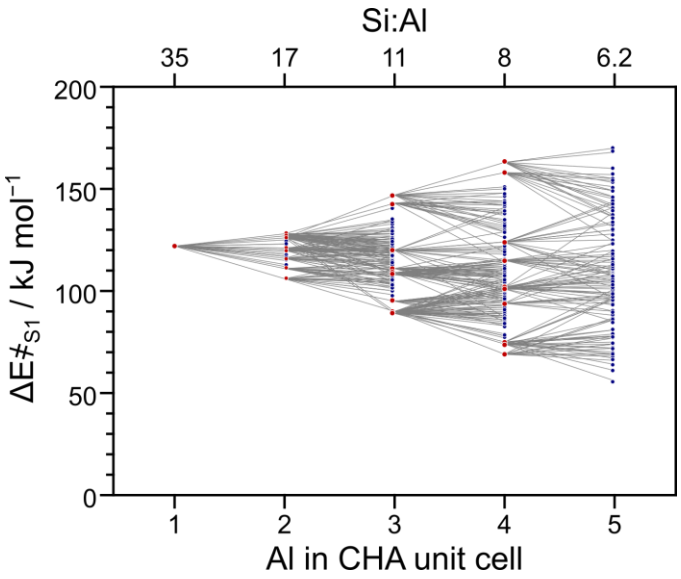

Figure S28. The spread in Step S1 energy barriers ($\Delta E^{\neq}_{S1}$) arising from each subsequent Al addition. Lines indicate structures generated from those with a higher Si:Al ratio to which Al were added (red dots).

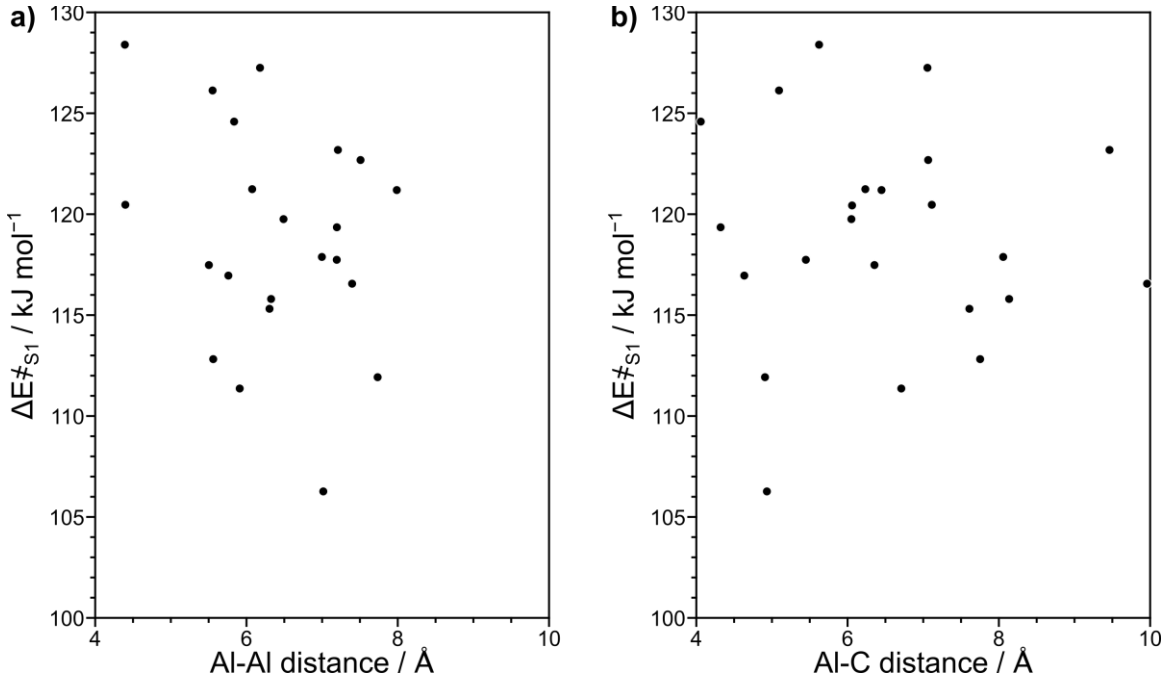

Figure S29. Intrinsic energy barrier for surface methylation ($\Delta E^{\neq}_{S1}$) with two Al in the CHA unit cell (Si:Al = 17) shown (a) as a function of distance between framework Al atoms and (b) as a function of the distance between the Al of the protonated site (not that being methylated) and the C of the Step S1 transition state.

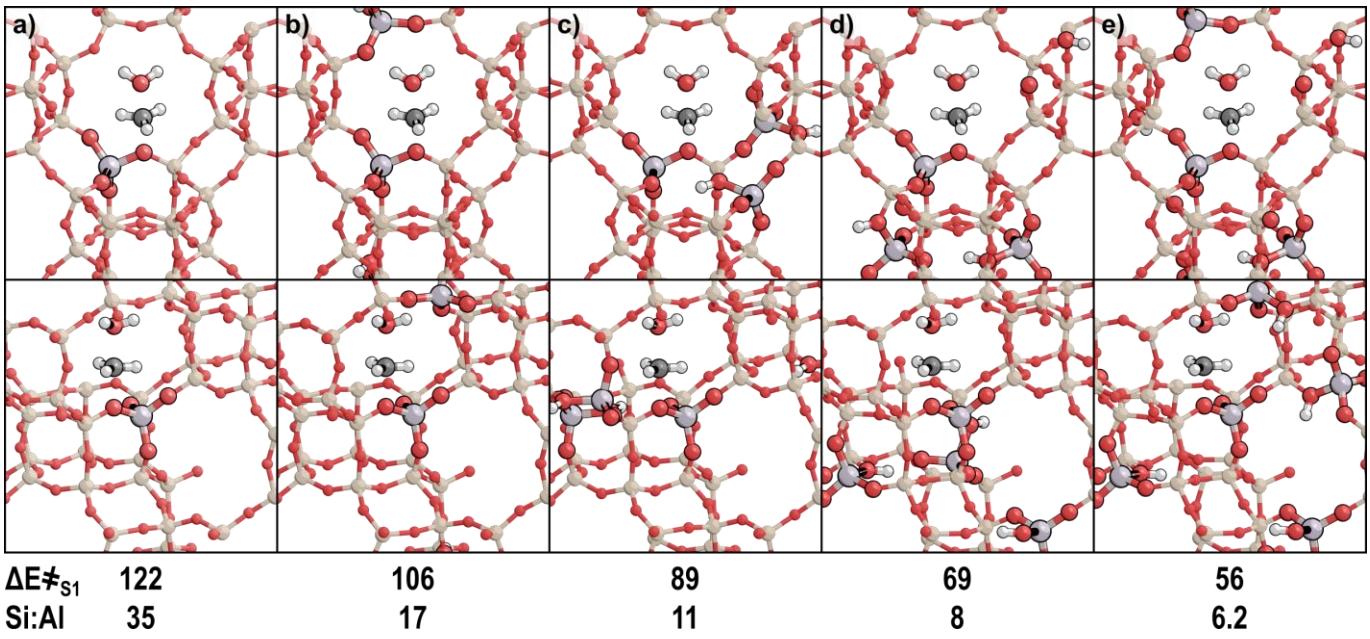

Figure S30. Structures for the lowest barrier surface methylation transition state on O3 (Step S1) with (a) one Al in the unit cell (Si:Al = 35), (b) two Al in the unit cell (Si:Al = 17), (c) three Al in the unit cell (Si:Al = 11), (d) four Al in the unit cell (Si:Al = 8), and (e) five Al in the unit cell (Si:Al = 6.2). The intrinsic energy barrier ($\Delta E^{\neq}_{S1}$) relative to a methanol monomer adsorbed to O3 in kJ mol^{-1} and Si:Al ratio are shown below each image.

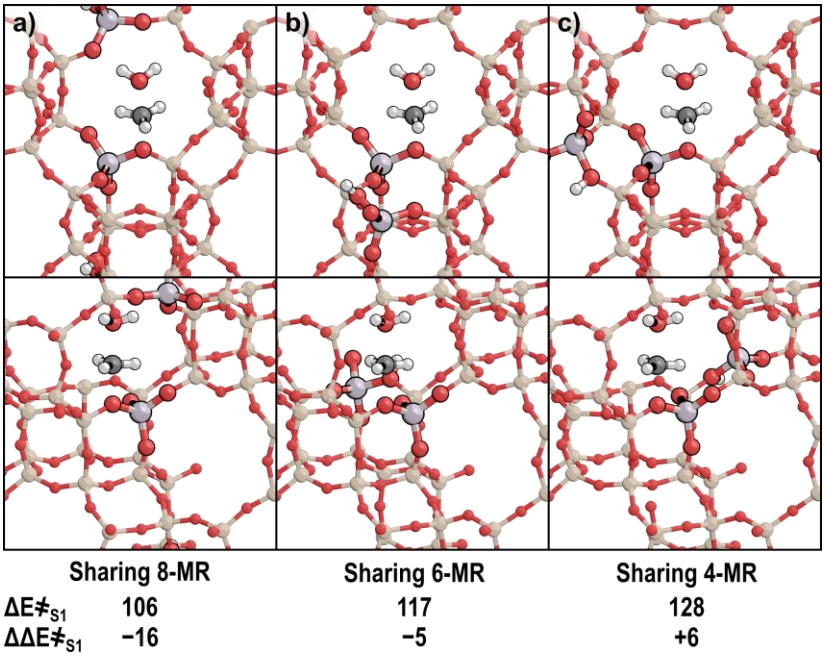

Figure S31. Exemplar structures for the surface methylation transition state on O3 (Step S1) with two Al in the unit cell where (a) the Al share an 8-MR around the transition state, (b) the Al share a 6-MR adjacent to the transition state, and (c) the Al share a 4-MR.

References

[1] G. Kresse, J. Hafner, *Phys. Rev. B* **1993**, *47*, 558–561.

[2] G. Kresse, J. Hafner, *Phys. Rev. B, Condens. Matter* **1994**, *49*, 14251–14269.

[3] G. Kresse, J. Furthmüller, *Comp. Mater. Sci.* **1996**, *6*, 15–50.

[4] G. Kresse, J. Furthmüller, *Phys. Rev. B* **1996**, *54*, 11169–11186.

[5] P. Kravchenko, C. Plaisance, D. Hibbitts, **2019**, *Preprint*, DOI 10.26434/chemrxiv.8040737.v3.

[6] P. E. Blöchl, *Phys. Rev. B* **1994**, *50*, 17953–17979.

[7] G. Kresse, D. Joubert, *Phys. Rev. B* **1999**, *59*, 1758–1775.

[8] S. Grimme, S. Ehrlich, L. Goerigk, *J. Comput. Chem.* **2011**, *32*, 1456–1465.

[9] S. Grimme, J. Antony, S. Ehrlich, H. Krieg, *J. Chem. Phys.* **2010**, *132*, 154104.

[10] J. P. Perdew, K. Burke, M. Ernzerhof, *Phys. Rev. Lett.* **1996**, *77*, 3865–3868.

[11] H. Jónsson, G. Mills, K. W. Jacobsen, in *Classical and Quantum Dynamics in Condensed Phase Simulations* (Eds.: B.J. Berne, G. Ciccotti, D.F. Coker), World Scientific, **1998**, pp. 385–404.

[12] G. Henkelman, H. Jónsson, *J. Chem. Phys.* **2000**, *113*, 9978–9985.

[13] G. Henkelman, H. Jónsson, *J. Chem. Phys.* **1999**, *111*, 7010–7022.

[14] W. C. Lu, C. Z. Wang, T. L. Chan, K. Ruedenberg, K. M. Ho, *Phys. Rev. B* **2004**, *70*, DOI 10.1103/PhysRevB.70.041101.

[15] M. DeLuca, P. Kravchenko, A. Hoffman, D. Hibbitts, *ACS Catal.* **2019**, *9*, 6444–6460.

[16] J. R. Di Iorio, A. J. Hoffman, C. T. Nimlos, S. Nystrom, D. Hibbitts, R. Gounder, *J. Catal.* **2019**, *380*, 161–177.

[17] D. A. McQuarrie, *Statistical mechanics*, University Science Books, Sausalito, Calif, **2000**.

[18] C. Baerlocher, L. B. McCusker, "Database of Zeolite Structures: http://www.iza-structure.org/databases.," can be found under http://www. iza-structure. org/databases, **2013**.

[19] A. Hoffman, M. DeLuca, D. Hibbitts, *J. Phys. Chem. C* **2019**, *123*, 6572–6585.

[20] S. Nystrom, A. Hoffman, D. Hibbitts, *ACS Catal.* **2018**, *8*, 7842–7860.

[21] W. Löwenstein, *Am. Mineral* **1954**, *39*, 92–96.

[22] R. E. Fletcher, S. Ling, B. Slater, *Chem. Sci.* **2017**, *8*, 7483–7491.

[23] S. Li, H. Li, R. Gounder, A. Debellis, I. B. Müller, S. Prasad, A. Moini, W. F. Schneider, *J. Phys. Chem. C* **2018**, *122*, 23564–23573.

[24] J. R. Di Iorio, C. T. Nimlos, R. Gounder, *ACS Catal.* **2017**, *7*, 6663–6674.

[25] J. R. Di Iorio, R. Gounder, *Chem. Mater.* **2016**, *28*, 2236–2247.

[26] C. Paolucci, A. A. Parekh, I. Khurana, J. R. Di Iorio, H. Li, J. D. Albarracin Caballero, A. J. Shih, T. Anggara, W. N. Delgass, J. T. Miller, et al., *J. Am. Chem. Soc.* **2016**, *138*, 6028–6048.

[27] J. S. Bates, R. Gounder, *J. Catal.* **2018**, *365*, 213–226.

[28] J. S. Bates, B. C. Bukowski, J. W. Harris, J. P. Greeley, R. Gounder, *ACS Catal.* **2019**, DOI 10.1021/acscatal.9b01123.

[29] W. Vermeiren, J. P. Gilson, *Top. Catal.* **2009**, *52*, 1131–1161.

[30] K. Tanabe, W. F. Hölderich, *Applied Catalysis A: General* **1999**, *181*, 399–434.

[31] H. van Koningsveld, *Acta Crystallogr. B Struct. Sci.* **1990**, *46*, 731–735.

[32] C. Baerlocher, L. B. McCusker, D. H. Olson, *Atlas of zeolite framework types*, Elsevier, **2007**.

[33] D. H. Olson, G. T. Kokotailo, S. L. Lawton, W. M. Meier, *J. Phys. Chem.* **1981**, *85*, 2238–2243.

[34] R. Gounder, E. Iglesia, *J. Am. Chem. Soc.* **2009**, *131*, 1958–1971.

[35] R. Gounder, E. Iglesia, *Acc. Chem. Res.* **2012**, *45*, 229–238.

[36] A. Bhan, R. Gounder, J. Macht, E. Iglesia, *J. Catal.* **2008**, *253*, 221–224.

[37] A. Janda, A. T. Bell, *J. Am. Chem. Soc.* **2013**, *135*, 19193–19207.

[38] C. Song, Y. Chu, M. Wang, H. Shi, L. Zhao, X. Guo, W. Yang, J. Shen, N. Xue, L. Peng, et al., *J. Catal.* **2017**, *349*, 163–174.

[39] Y.-H. Guo, M. Pu, B.-H. Chen, F. Cao, *Applied Catalysis A: General* **2013**, *455*, 65–70.

[40] S. Schallmoser, T. Ikuno, M. F. Wagenhofer, R. Kolvenbach, G. L. Haller, M. Sanchez-Sanchez, J. A. Lercher, *J. Catal.* **2014**, *316*, 93–102.

[41] C.-J. Chen, S. Rangarajan, I. M. Hill, A. Bhan, *ACS Catal.* **2014**, *4*, 2319–2327.

[42] J. Van der Mynsbrugge, A. Janda, S. Mallikarjun Sharada, L.-C. Lin, V. Van Speybroeck, M. Head-Gordon, A. T. Bell, *ACS Catal.* **2017**, *7*, 2685–2697.

[43] A. Janda, B. Vlaisavljevich, L.-C. Lin, S. Mallikarjun Sharada, B. Smit, M. Head-Gordon, A. T. Bell, *J. Phys. Chem. C* **2015**, *119*, 10427–10438.

[44] A. Janda, B. Vlaisavljevich, L.-C. Lin, B. Smit, A. T. Bell, *J. Am. Chem. Soc.* **2016**, *138*, 4739–4756.

[45] A. Corma, A. V. Orchillés, *Micropor. Mesopor. Mat.* **2000**, *35-36*, 21–30.

[46] Y. V. Kissin, *Catalysis Reviews* **2001**, *43*, 85–146.

[47] S. Mallikarjun Sharada, P. M. Zimmerman, A. T. Bell, M. Head-Gordon, *J. Phys. Chem. C* **2013**, *117*, 12600–12611.

[48] A. J. Jones, E. Iglesia, *Angew. Chem. Int. Ed. Engl.* **2014**, *53*, 12177–12181.

[49] A. J. Jones, R. T. Carr, S. I. Zones, E. Iglesia, *J. Catal.* **2014**, *312*, 58–68.

[50] R. T. Carr, M. Neurock, E. Iglesia, *J. Catal.* **2011**, *278*, 78–93.

[51] R. Gounder, A. J. Jones, R. T. Carr, E. Iglesia, *J. Catal.* **2012**, *286*, 214–223.

[52] P. G. Moses, J. K. Nørskov, *ACS Catal.* **2013**, *3*, 735–745.

[53] A. Ghorbanpour, J. D. Rimer, L. C. Grabow, *ACS Catal.* **2016**, *6*, 2287–2298.

[54] H. Chiang, A. Bhan, *J. Catal.* **2010**, *271*, 251–261.

[55] W. Knaeble, E. Iglesia, *J. Phys. Chem. C* **2016**, *120*, 3371–3389.

[56] J. Macht, M. J. Janik, M. Neurock, E. Iglesia, *J. Am. Chem. Soc.* **2008**, *130*, 10369–10379.

[57] C. Baerlocher, L. B. McCusker, "Database of Zeolite Structures," can be found under http://www.iza-structure.org/databases/, **2019**.

[58] Y. Zhi, H. Shi, L. Mu, Y. Liu, D. Mei, D. M. Camaioni, J. A. Lercher, *J. Am. Chem. Soc.* **2015**, *137*, 15781–15794.